*geosciences*

MDPI

*Article*

# The Influence of Thermal Differences and Variation of Cl–F–OH Ratios on Cu-Ni-PGE Mineralization in the Contact Aureole of the South Kawishiwi Intrusion, Duluth Complex

**Zsolt Benkó [1,2,*], Aberra Mogessie [2], Ferenc Molnár [3], Steven A. Hauck [4], Mark J. Severson [4] and Karl Ettinger [2]**

1 Isotope Climatology and Environmental Research Centre, Institute for Nuclear Physics, Hungarian Academy of Sciences, Bem tér 18/c, 4026 Debrecen, Hungary
2 Institute of Earth Sciences, University of Graz, Universitätsplatz 2, 8010 Graz, Austria; aberra.mogessie@uni-graz.at (A.M.); karl.ettinger@uni-graz.at (K.E.)
3 Geological Survey of Finland, Betonimiehenkuja 4, 02151 Espoo, Finland; ferenc.molnar@gtk.fi
4 Natural Resources Research Institute, University of Minnesota, 5013 Miller Trunk Highway Duluth, Minneapolis, MN 55811-1442, USA; shauck@nrri.umn.edu (S.A.H.); mseverso@nrri.umn.edu (M.J.S.)
* Correspondence: zsoltbenkoo@gmail.com; Tel.: +36-20-595-9363

Received: 9 October 2018; Accepted: 7 December 2018; Published: 12 December 2018




**Abstract:** In the contact metamorphic aureole of the Duluth Complex, Cu-Ni-PGE mineralization occurs locally up to 100 m from the intrusion-footwall contact (Spruce Road area), whereas elsewhere (Dunka Pit deposit) the footwall granite and metapelite (Serpentine deposit) are barren. This study aimed to understand the effect of temperature and halogen fugacity variations on the presence or absence of mineralization in these footwall units. The mafic mineral assemblages, two-pyroxene, titanium-in-quartz, and biotite-apatite thermometers indicate that temperatures could be as high as 920 °C in the mineralized areas of the footwall, whereas the maximum temperature was lower by about 100 °C in the unmineralized part of the intrusion. Variation of the halogen concentrations and fugacities was monitored with the analysis of halogen concentrations in biotite and apatite. Fluorine and chlorine concentrations in biotite increase as a function of the distance from contact in the mineralized drill core and decrease in the unmineralized zones. Chlorine concentrations in apatite increase parallel with the distance from contact in the mineralized zones, whereas fluorine concentrations show only minor variation. Concentrations of these elements may have had subtle effect on the partial melting in the footwall units and indirectly facilitated the infiltration of the sulfide liquid into the footwall.

**Keywords:** Duluth Complex; South Kawishiwi intrusion; Cu-Ni-PGE mineralization; contact metamorphism; two-pyroxene thermometry; titanium-in-quartz thermometry; halogen fugacity

## 1. Introduction

Interaction between voluminous mafic intrusions with country rocks results in the formation of thick contact metamorphic zones, such as in Bushveld Complex, South Africa; Portimo Complex, Finland; and East Bull Lake Intrusive Suite, Canada [1,2]. The interaction may generate partial melting and circulation of hydrothermal fluid flow in the footwall of large igneous complexes, as seen in Sudbury Igneous Complex [3–7], and injection and assimilation of partial melts and volatiles from the footwall rocks [8–10]. These processes also influence the transport and crystallization of base and precious metals, and accordingly, the formation of Cu-Ni-PGE sulfide deposits in the contact

zones or in the offset position around the mafic intrusions. The mineralization of footwall/country rock is commonly enriched in Cu and PGE (platinum-group elements) when compared to the mafic intrusion [1,2] and may form economically significant, exploitable orebodies (e.g., McCreedy West, McCreedy East, Broken Hammer deposits in the footwall of the Sudbury Igneous Complex [3–5]; Sandsloot mine, Platreef, Bushveld [11]). Therefore, it is essential to understand the geochemical and physical processes in the footwall rocks of layered complexes during the contact metamorphism.

In the contact-metamorphosed granitic footwall of the South Kawishiwi intrusion, Duluth Complex, a Cu-Ni-PGE-Au mineralization (0.5% Cu and 900 ppb Pt + Pd + Au) at the Spruce Road area has been reported in the 90s [12,13]. It has been suggested that these anomalously high ore grades in the charnockite (contact metamorphosed, orthopyroxene-bearing granite) are probably associated with partial melting and/or hydrothermal fluid flow in the footwall [13,14]. According to that model, partial melting and hydrothermal fluid flow can be related to principal magma flow channels at the base of the South Kawishiwi intrusion. New sulfide droplets were formed, settled, and locally pooled in the magma channels at the base of the intrusion, due to the incorporation of the partially molten granitic footwall into the mafic magma [15]. Partial melting of the charnockitic and metapelitic footwall during contact metamorphism, as well as sulfide assemblages in the footwall of the Spruce Road deposit, were investigated [16–19]. Partial melting of the footwall up to 125 m from the intrusion–footwall contact was documented at the Spruce Road deposit [16,20–22] and showed that partial melting played a significant role in the filtration of the sulfide liquid downward into the footwall of the intrusion. Nevertheless, no evidence has been put forward to prove temperature anomalies between different sections in the contact aureole of the South Kawishiwi intrusion that could reinforce the role of the temperature anomalies in the distribution of Cu-Ni-PGE sulfide ore. A drawback of such a comparison is that, except in a few cases, drilling was usually terminated when the intrusion/footwall was reached. Systematic variation in the halogen concentration of syn-metamorphic biotite and apatite was also observed [18] and assumed that increasing halogen content (F) of the syn-metamorphic fluids may have also contributed to the partial melting, thus creating channel ways for transportation of sulfide droplets into the footwall. In addition, chlorine is a principal ligand in aqueous solutions during base metal transport and under certain conditions in precious metal (PGE, Au) transport [23,24].

One of the major aims of this work is to demonstrate the occurrence of temperature anomalies in the contact aureole of the South Kawishiwi intrusion and their role in formation of footwall mineralization by comparing mineralized and unmineralized segments in the footwall. Temperatures during contact metamorphism are estimated based on equilibria of ferromagnesian mineral assemblages [25], two-pyroxene thermometry [26], titanium-in-quartz thermometry [27], and apatite-biotite thermometry [28]. Another purpose of this study was to evaluate the effect of halogens (F, Cl) on the formation of sulfide mineralization in the footwall by investigation of the halogen fugacity ratios in biotite and apatite.

## 2. Regional Geology

### 2.1. Setting and Composition of the Duluth Complex

The Duluth Complex is hosted by the Mezoproterozoic (1.1 Ga) Midcontinent rift system that stretches from north Kansas to northern Minnesota (Figure 1a) [29]. The half graben of the aborted rift zone in the area of Duluth is filled by sediments and tholeiitic intrusive–volcanic rocks of the Keweenawan Supergroup. The intrusions of the Duluth Complex belong to four magmatic rock series; *Early Gabbro Series*, *Felsic Series*, *Anorthositic Series*, and *Layered Series*, which intrude between the footwall Neoarchean (2.7 Ga) granitic and Early Proterozoic metapelitic rocks and the hanging-wall syngenetic mafic volcanic and anorthositic rocks. Among these, only some intrusions of the *Layered Series* contain economically important Cu-Ni-PGE mineralizations [30]. The *Layered Series* comprises nine sill-like, individual intrusions (Figure 1b). Lithologically, the intrusions consist of cumulate, locally pegmatitic textured troctolite, anorthositic troctolite, gabbro, and melatroctolite [30,31].

Cu-Ni-PGE sulfide mineralization is currently only known in the basal zones of the South Kawishiwi, Bathtub (BTI), and Partridge River intrusions (PRI) (Figure 1c). The co-genetic *Anorthositic Series* and effusive basaltic rocks form the hanging wall of these intrusions. Footwall rocks are the Neoarchean granitic and monzonitic rocks of the Archean Giants Range batholith, the Early Proterozoic Biwabik Iron Formation, and the metapelitic Virginia Formation [29].

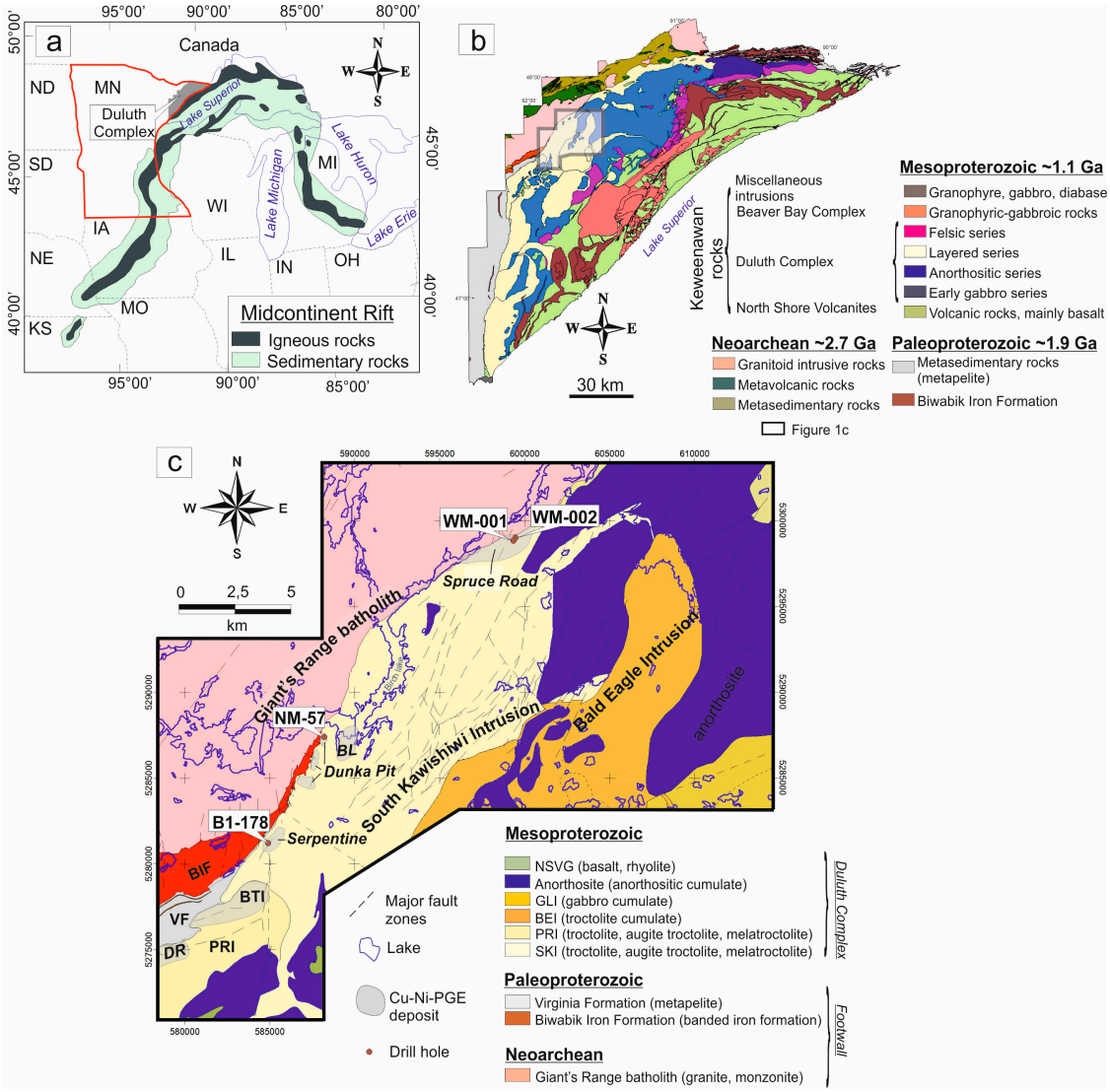



**Figure 1.** (**a**) The Midcontinent Rift system in North–America (significantly modified after [32]). (**b**) Geology of the Duluth Complex (the map is slightly modified after [30]). The South Kawishiwi intrusion studied in this work is highlighted by a black polyline. (**c**) Geology of the South Kawishiwi intrusion and its surroundings. Abbreviations: BL—Birch Lake Deposit, DR—Dunka Road Deposit, BTI—Bathtub intrusion, PRI—Partridge River intrusion, SKI—South Kawishiwi intrusion, BEI—Bald Eagle intrusion, GLI—Gabbro Lake intrusion, NSVG—North Shore Volcanic Group, VF—Virginia Formation.

## 2.2. Geology and Mineralization of the South Kawishiwi Intrusion

The arc-shaped South Kawishiwi intrusion (Figure 1b) consists mainly of troctolitic cumulates intercalated with cyclic anorthositic and ultramafic horizons. The intrusion dips gently to the southeast.

Sulfide mineralization in the South Kawishiwi intrusion (~1.5 billion tons cumulated resources; average ore grades are 0.5% Cu, 0.2% Ni, and 700 ppb Pt + Pd + Au [32]) is confined to the bottom 100–300 m basal mineralized zone of the intrusion. The overlying several hundred meter thick

homogeneous unit has mainly troctolitic and anorthositic composition. The sulfide mineralization in the basal zone consists of disseminated intercumulus of chalcopyrite, cubanite, pyrrhotite, pentlandite, and bornite, but locally, small, semi-massive pyrrhotite-pentlandite-chalcopyrite pods also occur [20,30,33].

Two different types of mineralization have been distinguished in the South Kawishiwi intrusion, based on extensive field mapping and analysis of the geochemical data [14]. One type, informally called "open style mineralization" is depleted in precious metals, having a total precious metal content (TPM = Pt + Pd + Au) of generally less than 1 ppm. It has a relatively thick vertical extent (~450 m) with increasing Cu and Ni concentrations towards the footwall. The other, informally named "confined type mineralization", has only a maximum 150 m vertical extent and the total precious metal content is significantly higher (up to 10 ppm). Base and precious metal contents increase from the top to the bottom of the mineralized segment of the intrusion.

The "open style mineralization" is considered as the first generation of magmatic sulfide deposits, whereas the "confined style mineralization" represents magmatic sulfide ores deposited from a late-stage, more continuous pulse of magma [15,34].

### 2.3. Composition of the Footwall Beneath the South Kawishiwi Intrusion

North of the Serpentine deposit (Figure 1c), the 2.7 Ga Giants Range batholith, part of the Wawa sub-province of the Canadian Shield, forms the footwall of the South Kawishiwi intrusion. The Giants Range batholith is lithologically heterogeneous, but rocks adjacent to the intrusion are predominantly equigranular or porphyritic, biotite- and hornblende-bearing diorite, adamellite, monzonite, and monzodiorite [35–37]. In the contact aureole, the monzonitic and granitic rocks are charnockized; biotite and hornblende are replaced by augite and enstatite respectively, and feldspars are partly recrystallized. Locally, cuspate-formed quartz at the corners of plagioclase grains, euhedral orthopyroxene in contact with quartz, and plagioclase overgrowths on strained, inclusion-rich plagioclase [16] indicate partial melting of the footwall rocks during the emplacement of the intrusion. Temperatures in the footwall during the contact metamorphism reached 800 °C [15] and pressure was between 1.5–1.8 kbar along the contact at the northwestern part the South Kawishiwi intrusion [36]. Results of fluid inclusion studies indicate that the peak metamorphic fluid was almost pure $CO_2$ that trapped between 1.6–2 kbar pressure and 810–920 °C temperature [38]. Low temperature (120–165 °C), heterogeneous $CO_2$–$H_2O$–NaCl and $CH_4$–$N_2$–$H_2O$–NaCl, as well as high salinity (21.6–28.8 NaCl + $CaCl_2$ equiv. wt. %) but low temperature (90–160 °C) fluids partly remobilized base metals after the emplacement of the intrusion. However, this remobilization cannot be connected to the cooling of the Duluth Complex as the estimated pressure for these fluid inclusion assemblages is lower than 650 bars [39].

Three different types of sulfide mineralization can be distinguished in the contact aureole beneath the South Kawishiwi intrusion at the Spruce Road area (WM-001, WM-002 drill cores) [18,21]. In the proximity of the intrusion/footwall contact (10–15 m), the mineralization is semi-massive, net-textured, predominated by pyrrhotite, pentlandite, and chalcopyrite. Platinum group minerals (PGM), such as sperrylite, are rare. In the distal zones (15–100 m), the ore mineralization is disseminated and dominated by bornite and chalcopyrite. PGMs (moncheite) and other precious (native gold, native silver, hessite) and base metal minerals (galena, sphalerite, parkerite, greenockite, etc.) in this assemblage are abundant. One previous study [22] has presented textural, sulfur isotopic, and geochemical evidence (PGE + Au analyses) suggesting that the formation of these mineral assemblages is: (1) related to the partial melting of the monzonitic/granitic footwall, and (2) derived probably by fractional crystallization of sulfide liquid that penetrated from the intrusion into the partially molten footwall, but fluids may have also played a significant role in the variation of PGE concentration as a function of distance from the contact. The third type of mineralization is the result of subsequent hydrothermal processes that remobilized Cu from the primary mineralization into late chalcopyrite bearing veins,

which are surrounded by actinolite, chlorite, quartz, calcite, prehnite, and pumpellyite bearing alteration [39]. These late veins also locally occur in the intrusion [9].

South of the Birch Lake deposit (Figure 1c), the Giants Range batholith is unconformably overlain by the Early Proterozoic Biwabik Iron Formation. The Biwabik Iron Formation is conformably overlain by the Virginia Formation that forms the direct footwall of the South Kawishiwi intrusion in this area. The Virginia Formation is comprised of graphite- and pyrite-bearing argillite, siltstone, and greywacke, interbedded by chert and limestone layers [40]. Where the Virginia Formation was intruded and partly assimilated by the mineralized intrusions (South Kawishiwi-, Partridge River-, Bathtub intrusions; Figure 1c), it provided a local sulfur and also semimetal source for the pyrrhotite-dominated massive sulfide mineralization at the bottom of the intrusions [14,37,40–44]. Partial melting of the Virginia Formation is discussed in other studies [15,16]. According to these observations, the partially molten meta-argillite contains 2.4 modal percent leucosome (segregated partial melt) that formed within a matrix consisting of 40.5% *in-situ* newly formed partial melt (neosome) and 57.1% cordierite + plagioclase framework, which was not affected by the partial melting. The neosome crystallized to biotite + quartz + plagioclase ± K-feldspar. Small micropores formed during initiation of partial melting coalesce into small elliptical micro-leucosomes. In the next phase, these micropores grow and form an en echelon array of microleucosomes. Finally, the microleucosomes with high aspect ratios (the ratio of length to width ~30) fill up a network of interconnected fractures.

## 3. Sampling and Methodology

Samples were collected from the Drill Core Library Minnesota Department of Natural Resources, Minerals Division in Hibbing. Footwall rocks were sampled at three deposits, in three vertical drill cores (Figure 1c). The mineralized charnockite was sampled in the WM-002 drill core at the Spruce Road deposit, whereas the barren charnockitic footwall is represented by samples from the NM-57 drill core at the Dunka Pit deposit. The unmineralized metapelite samples are from the B1-178 drill hole at the Serpentine deposit. Additional aspects of selecting drill cores for sampling were as follows: (1) the apparent thickness of the drilled footwall (2) availability of previous data for the studied deposits and (3) accessibility of the drill cores. An aim of the sampling was to set up halogen and temperature profiles in various footwall rock lithologies, mineralized and unmineralized, in the possible maximum vertical extent. From the samples, altogether 72 polished thin sections have been prepared and studied under transmitted and reflected light microscopes.

A JEOL 6310 SEM (Scanning Electron Microscope) equipped with a Link ISIS energy dispersive system and a Micro–Spec wavelength dispersive system at the Institute of Earth Sciences, University of Graz was used for analysis of the composition of minerals. Accelerating voltage for silicates and phosphates was 15 kV and the probe current was 5 nA. Detection limits are 0.1–0.2 wt. % for Energy Dispersive X-ray (EDX) and 0.03 wt. % for WDX (Wavelength Dispersive X-ray) analysis. Chlorine concentrations in biotite and apatite were measured with EDS, whereas fluorine concentrations were measured with WDS. The standards were atacamite for chlorine and apatite S3 Wilberforce for fluorine. The error of the F and Cl analysis in biotite are around 15% and 10–50%, respectively. Analysis of halogens in biotite as well as in other minerals is difficult, as these elements diffuse easily from the crystal lattice even after short-time heating of the sample with the electron beam of the SEM. The errors will be therefore necessarily high especially if the halogen concentrations are close to the detection limit. Errors for F and Cl in apatite are around 3% and 10%, respectively.

Titanium in quartz analysis was performed using the JEOL Superprobe JXA–8200 at the Eugen Stumpfl Electron Microprobe Laboratory of the Universitätszentrum für Angewandte Geowissenschaften (UZAG), Steiermark, and at the Mining University of Leoben, operated at 15 kV accelerating voltage, 50 nA beam current, ~1µm beam diameter, and counting times of 100 and 300 s for peak and backgrounds, respectively. Reported precisions are based on cumulative counting statistics.

## 4. Results

### 4.1. Petrography

#### 4.1.1. Unmineralized Charnockite at the Dunka Pit Deposit (NM-57 Drill Core)

The charnockite is both compositionally and texturally heterogeneous in the NM-57 drill core (Figure 2). Major constituents of the medium-grained (500–1000 μm) charnockite are plagioclase, orthopyroxene, clinopyroxene, biotite, K-feldspar, quartz, titanomagnetite (complex Fe-Ti-oxide crystals with magnetite and ilmenite exsolution lamellae), and apatite. The texture of the charnockite is hetero-granular granoblastic. Locally subhedral feldspar crystals (200–400 μm) form a polygonal texture. Pyroxene and biotite occur in various textural forms. Orthopyroxene (250–750 μm) encloses fine-grained (~100 μm) corroded biotite crystals, indicating incomplete breakdown of biotite during peritectic reactions. This early resorbed biotite (biotite I) is presumably the remnant of rock-forming magmatic biotite from the granite protolith (Figure 3a,b). The second generation of euhedral or subhedral rosette-like, reddish-brown biotite (300–600 μm) replaces either orthopyroxene or forms flakes between plagioclase crystals (Figure 3c). This second generation of biotite (biotite II) most likely crystallized as a result of melt-solid reaction [45] or by melt-back reaction. Clino and orthopyroxene (250–750 μm) is subhedral or euhedral (Figure 3d), and in some rare cases has an amphibole rim. Apatite is intimately intergrown with the flakes of biotite II (Figure 3e–g). Occurrences of films and pools of symplectite coronas around feldspars and patches in the contact of quartz and feldspar indicate partial melting in the charnockitic host up to 125 m from the intrusion-footwall. Coalescence of partial melt droplets into fracture filling masses was only locally observed up to 15 m from the intrusion-footwall contact.

The granite was intruded by mafic sills, aplite, and pegmatite dykes (Figure 2) prior to the charnockitization i.e., the formation of the South Kawishiwi intrusion. These sills are mineralogically identical with the host granite, only the modal proportion of mafic minerals is higher (visual estimation) resulting in a darker color of the rocks. In the proximity of the intrusion-footwall, intense recrystallization and abundant partial melting features make the distinction between the host charnockite and the sill difficult. In some sills in the close proximity to the South Kawishiwi intrusion, evidence of in situ melting (in situ melt—partial melt that remained in contact with its residuum) attributes are common. The *in-source* leucosome veins (e.g., product of crystallization of a partial melt that has migrated away from the place where it has been formed but is still within the source rock—[45]) are feldspar rich.

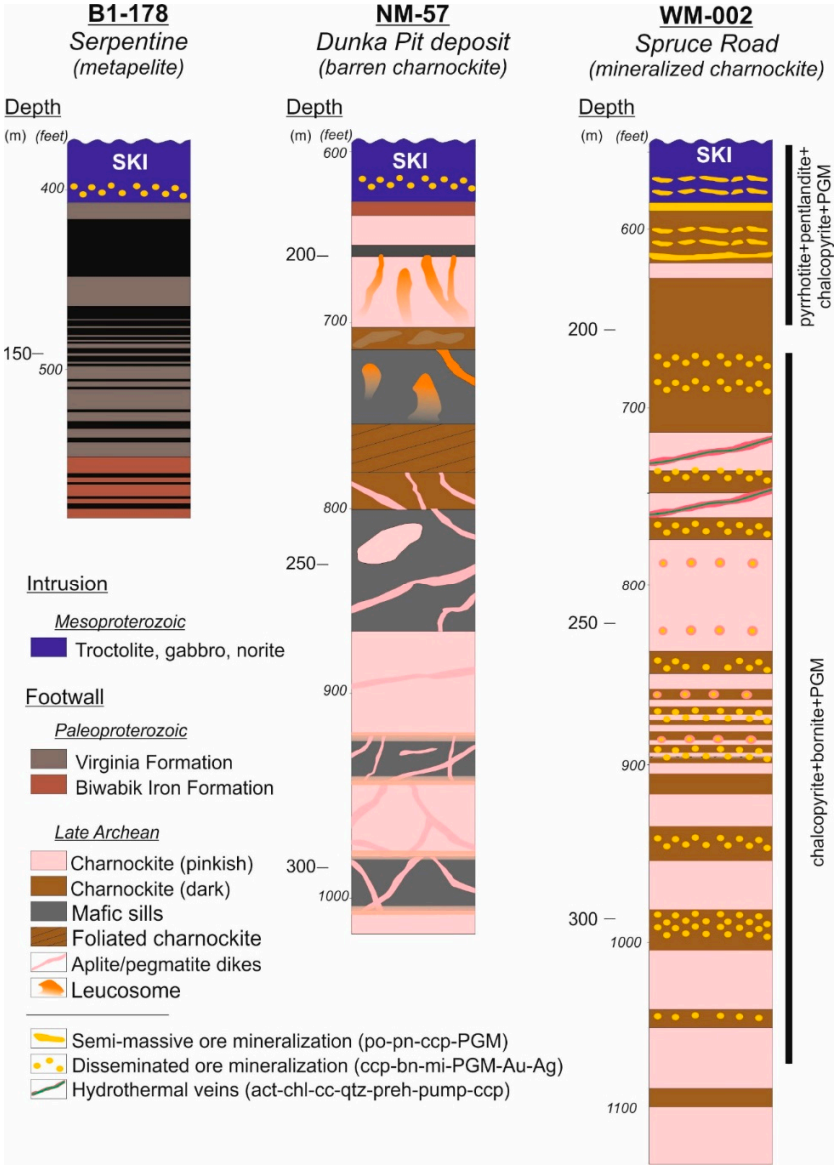



**Figure 2.** Graphic logs of the footwall part of the sampled drill cores at the Serpentine, Dunka Pit and Spruce Road deposits. Abbreviations: SKI—South Kawishiwi intrusion, po—pyrrhotite, pn—pentlandite, ccp—chalcopyrite, bn—bornite, mi—millerite, act—actinolite, chl—chlorite, cc—calcite, qtz—quartz, preh—prehnite, pump—pumpllyite, PGM—platinum group minerals).

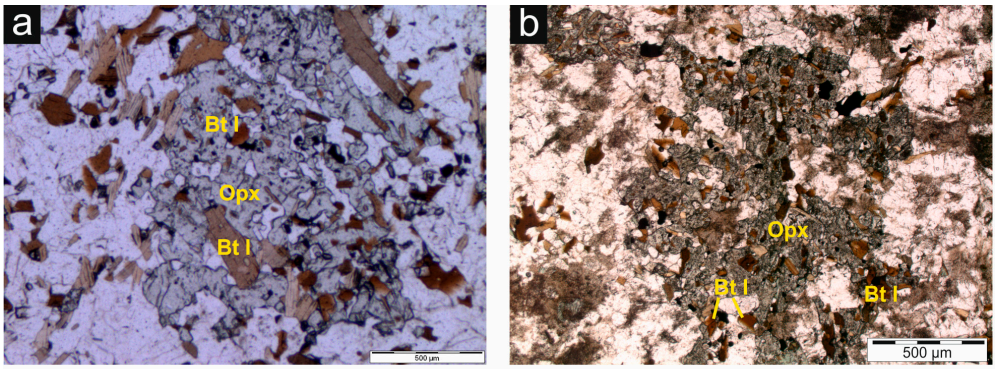



**Figure 3.** *Cont.*

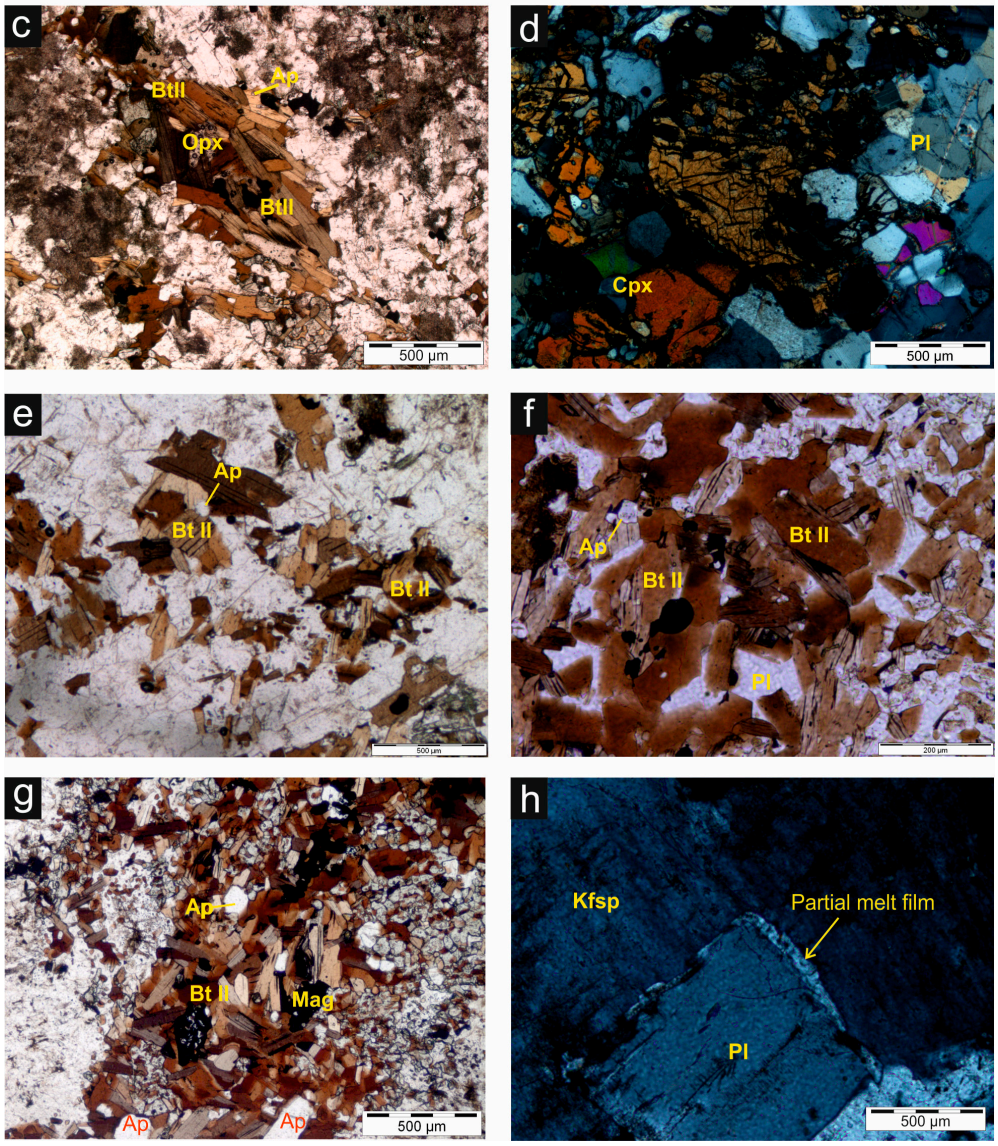



**Figure 3.** Texture of the unmineralized charnockite in the NM-57 drill core (Dunka Pit deposit). (**a**,**b**) Residual biotie I (Bt I) replaced by orthopyroxene (opx) (PPL image). (**c**) Orthopyroxene replaced by subhedral-euhedral biotite (Bt II) (PPL image). (**d**) Euhedral ortho-and clinopyroxene, 5 m from the contact (XPL image). (**e**–**g**) Euhedral biotite II (Bt II) intergrown with euhedral apatite (Ap). (**h**) Partial melt film between feldspars (XPL image).

#### 4.1.2. Mineralized Charnockite at the Spruce Road Deposit (WM-002 Drill Core)

The charnockite in the footwall of the South Kawishiwi intrusion at the Spruce Road deposit is lithologically homogeneous: no aplite, pegmatite, or mafic sills are found in the WM-002 drill core. Texturally, the charnockite is porphyroblastic which reflects the porphyric texture of the protolith monzonite.

The footwall rock units mainly consist of plagioclase, ortho- and clinopyroxene, and biotite (Figure 4). Accessory minerals are magnetite, +/− ilmenite, apatite, and titanite. Plagioclase porphyroblasts (1–2 mm) developed antiperthite exsolution of K-feldspar upon cooling after the emplacement of the intrusion. Adjacent to the contact these have sieve textures due to partial melting. Ortho- and clinopyroxene is present in the footwall up to 125 m from the contact. Euhedral or subhedral (500–700 µm) enstatite and augite occur between feldspar porphyroblasts. Enstatite is locally replaced

by biotite, whereas augite is locally replaced by amphibole. In the pyroxene crystals, no exsolution lamellae were observed.

Two generations of biotite were observed. The presence of corroded magmatic biotite I (20–50 µm) as a relict of an incomplete peritectic reaction was observed in only a few samples. Occurrences of the rosette-like biotite II (50–200 µm), which replaces either orthopyroxene or forms flakes between feldspar porphyroblasts (Figure 4f), is rather ubiquitous, but the modal proportion of biotite II varies abruptly along the drill core from <1% locally up to 40–50%. Very high modal proportions of biotite II are characteristic in partial melts associated with plagioclase, apatite, and magnetite (Figure 3f).

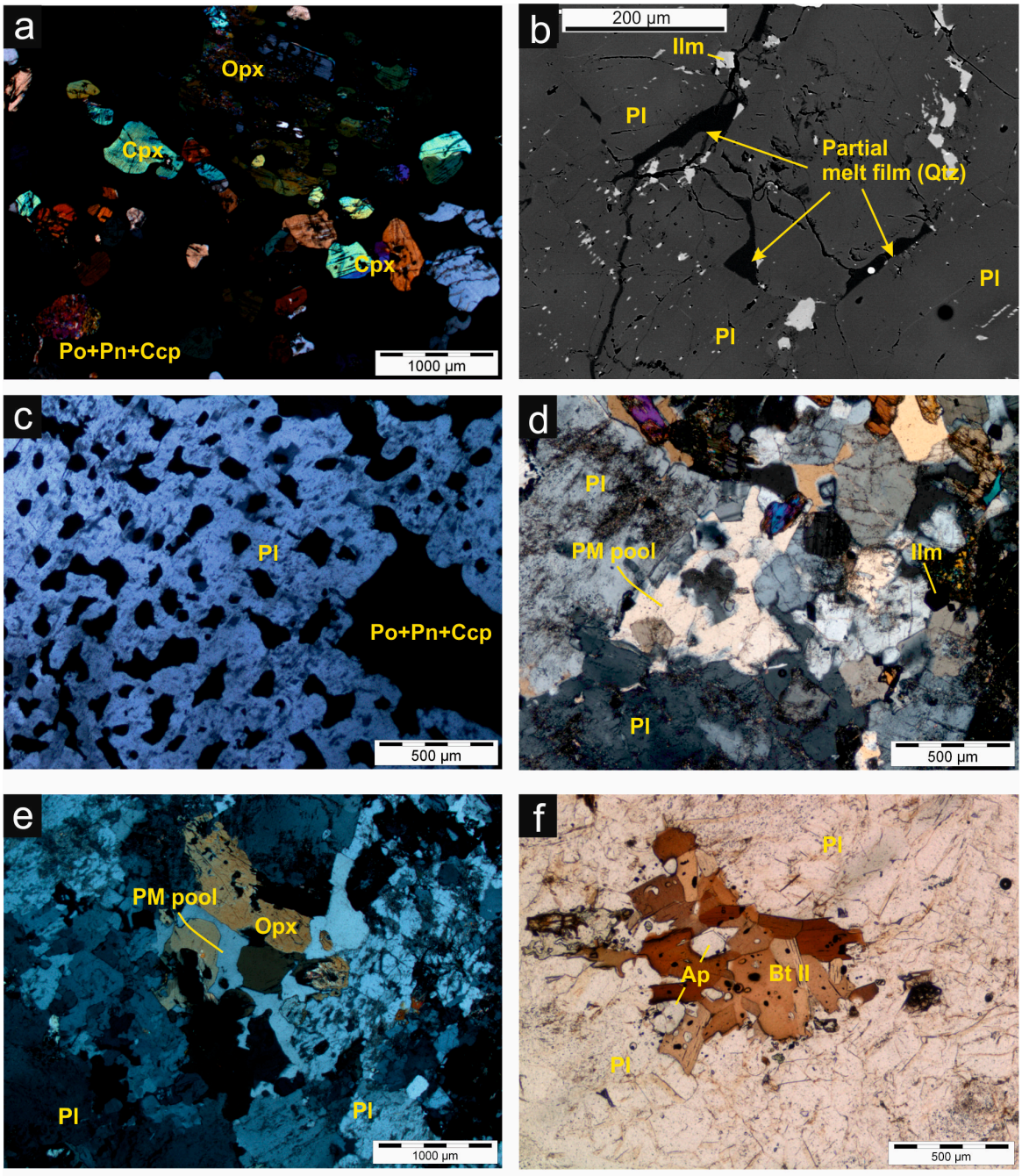



**Figure 4.** *Cont.*

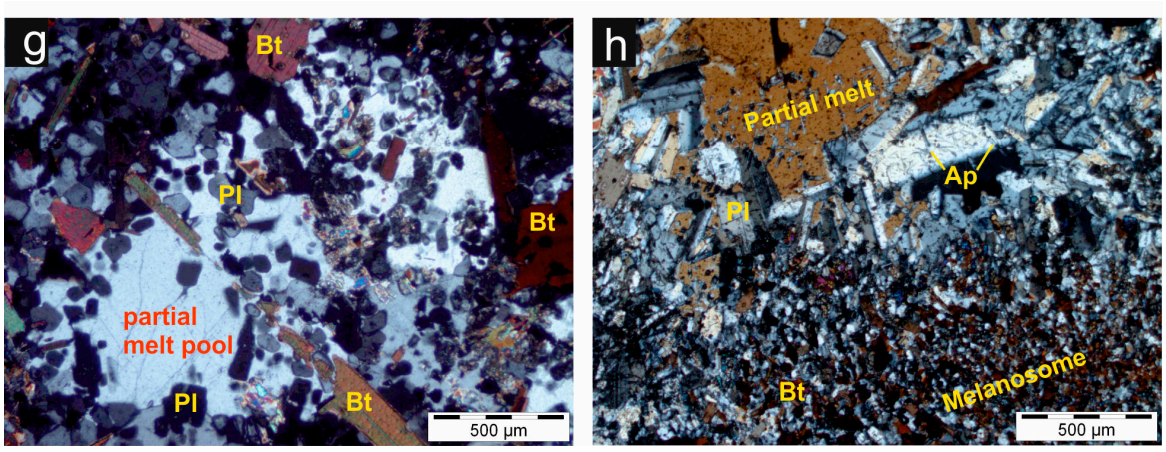



**Figure 4.** Texture of the charnockite in the WM-002 drill core (Spruce Road deposit). (**a**) Net-texture of Euhedral ortho- and clinopyroxene crystals in a sulfide matrix, composed of pyrrhotite (Po), Pentlandite (Pn), and chalcopyrite (Ccp) (XPL image). (**b**) Partial melt film between plagioclase porphyroblasts. The partial melt crystallized to quartz ± K-feldspar ± plagioclase (SEM image). (**c**) Sieve textured feldspar partially replaced by sulfide minerals (pyrrhotite, pentlandite, and chalcopyrite) (XPL image). (**d**,**e**) Partial melt pocket—note the euhedral clinopyroxene crystal and the quadrant plagioclase crystals. The partial melt crystallized to quartz (white) (XPL image). (**f**) Euhedral biotite II intergrown with euhedral apatite (PPL image). Texture of the metapelite in the B1-178 drill core (Serpentine deposit). (**g**) Partial melt pocket—note the euhedral biotite crystals and the quadrant plagioclase crystals. The partial melt crystallized to quartz (light blue) (XPL image). (**h**) Partial melt in the metapelite. The fine-grained melanosome is rich in biotite and plagioclase. The partial melt crystallized to coarse-grained plagioclase, biotite, and quartz. Note the abundant euhedral apatite crystals as inclusions in plagioclase (XPL image).

Apatite occurs as an accessory mineral in small amounts (<1%) in the charnockite. Needle-like or columnar crystals (100–300 µm) form inclusions in recrystallized feldspars or as individual crystals between recrystallized or porphyroblastic feldspars. The intergrowth of apatite with recrystallized plagioclase, as well as with biotite II in the neosome, suggests that apatite crystals grew during partial melting of granitoids in the footwall (Figure 4f).

Evidence for partial melting is abundant in the entire studied section of the drill core. The evidence is as follows:

(1) Ortho- and clinopyroxene have well-crystallized crystal faces against quartz and feldspars that occur between plagioclase porphyroblasts (Figure 4a). Euhedral crystal faces against the quartz and feldspar that crystallized from the partial melt prove that pyroxene grew during the contact metamorphism.

(2) Quartz occurs with cuspate crystal faces interstitially between plagioclase porphyroblasts (Figure 4b).

(3) Plagioclase forms mosaic textured aggregates, particularly in samples adjacent to the intrusion (Figure 4c). According to the experiments on plagioclases at 2 kbar pressure, this texture indicates dry partial melting at high temperature (880 °C). Overgrowth textures, which occur on corroded and strained residual plagioclase crystals, are also abundant in the entire section.

(4) Partial melt films and pools that crystallized to quartz + plagioclase appear between feldspar porphyroblasts (Figure 4d,e).

(5) Large euhedral biotite (500–1000 µm) crystals, dominant in the distal part of the studied drill core (50–100 m from the intrusion-footwall contact), have smooth crystal faces against quartz, indicating growth of the biotite II in the presence of melt phase.

(6) Symplectitic intergrowth of quartz and plagioclase.

Mineralization in the proximal 10–15 m section of the footwall is pyrrhotite-pentlandite-chalcopyrite-PGM-rich and the texture of the mineralization is semi-massive, net-textured (Figure 4a,c). Sulfide minerals often fill in the empty space that remained after the melting of the primary feldspars. It was suggested by [21,22] that sulfide mineralization in this proximal part of the drill core was formed by the infiltration of sulfide liquid from the basal zones of the troctolitic intrusion. In the distal 15–100 m section of the footwall, the mineralization is rich in chalcopyrite + bornite + PGM. Sulfide minerals occur together with crystallized partial melt pools, but a major difference compared to the proximal part is that in this distal zone biotite II is always present around the sulfide minerals.

#### 4.1.3. Unmineralized Metapelitic Hornfels at the Serpentine Deposit (B1-178 Drill Core)

The Virginia Formation adjacent to the South Kawishiwi intrusion appears as a grey, fine-grained (<250 μm) metapelite with a granoblastic texture. The major constituents of the metapelitic hornfels are plagioclase (~100 μm), orthopyroxene (~100 μm), cordierite (~150 μm), biotite (50–500 μm), K-feldspar (250–500 μm), and quartz (250–500 μm). Apatite, pyrrhotite, chalcopyrite, graphite, and magnetite occur as accessory phases. Petrographic indications of partial melting are abundant close to the intrusion-footwall in the studied section of the B1-178 drill core. For the in situ partial melt patches (a partial melt that ponds and does not mobilize at the site of the melting; Figure 4g) [45], biotite and plagioclase are enclosed by quartz and K-feldspar that crystallized last. Smooth crystal faces of plagioclase, biotite, and cordierite were interpreted as products of crystallization in a diatexite migmatite [45]. Orthopyroxene is euhedral and is interpreted as the product of the melting of biotite in a diatexite migmatite [16,17]. Biotite and apatite are generally intimately intergrown or apatite occurs as euhedral crystals in pockets which were formed by the crystallization of partial melt droplets (Figure 4h). Locally, in-source partial melt veins are composed of subhedral quartz, plagioclase, and K-feldspar (250–1000 μm), with abundant apatite crystals. In the partial melt veins, elongated biotite and pyroxene crystals are aligned in a parallel–subparallel direction, indicating flow direction of the partial melt.

### *4.2. Mineral Chemistry*

#### 4.2.1. Pyroxene

Representative compositions of pyroxene crystals used for the two-pyroxene thermometry [26] are given in Table 1. For estimation of the temperature during contact metamorphism, euhedral, inclusion-free, unaltered ortho- and clinopyroxene crystals that are in textural equilibrium were selected. Temperature calculations at the Spruce Road deposit (mineralized charnockite samples) have been carried out in two samples, 15 m (sample Z2-29) and 97 m (sample Z2-60) beneath the intrusion-footwall contact. Orthopyroxene in both samples is enstatite, ranging in composition from $En_{0.64–0.65}Fe_{0.24}Wo_{0.04–0.02}$ (14 m from the intrusion-footwall contact) to $En_{0.75–0.77}Fe_{0.26–0.28}Wo_{0.01}$ (97 m from the intrusion-footwall contact). Clinopyroxene is augite and compositions range from $En_{0.4–0.45}Fe_{0.09–0.13}Wo_{0.39–40}$ (15 m from the intrusion-footwall contact) to $En_{0.42–0.43}Fe_{0.09}Wo_{0.42–0.43}$ (97 m from the intrusion-footwall contact).

At the Dunka Pit deposit, two samples were selected, Z-162 and Z-169, at 68 m and 120 m distance from the intrusion-footwall contact, respectively. Orthopyroxene compositions in the two samples were $En_{0.62}Fe_{0.35}Wo_{0.03}$ and $En_{0.62–0.64}Fe_{0.32–35}Wo_{0.01}$, respectively. Clinopyroxene compositions in sample Z-162 were $En_{0.41}Fe_{0.10}Wo_{0.42}$ and in sample Z-169 were $En_{0.42}Fe_{0.09}Wo_{0.43}$.

**Table 1.** Representative electron microprobe analyses of pyroxene compositions.

| **Deposit/Drill Core** | **Spruce Road/WM-002** | | | | | **Dunka Pit Deposit** | | | | | | | |
|---|---|---|---|---|---|---|---|---|---|---|---|---|---|
| Sample | Z2-29 | Z2-29 | Z2-60 | Z2-60 | Z2-60 | Z-162 | Z-162 | Z-162 | Z-162 | Z-169 | Z-169 | Z-169 | Z-169 |
| Depth (m) | 126 | 196 | 293 | 293 | 293 | 68 | 68 | 68 | 68 | 120 | 120 | 120 | 120 |
| Mineral | *cpx* | *opx* | *cpx* | *opx* | *opx* | *cpx* | *cpx* | *opx* | *opx* | *cpx* | *cpx* | *opx* | *opx* |
| *wt%* | | | | | | | | | | | | | |
| $SiO_2$ | 52.76 | 55.24 | 53.34 | 52.93 | 53.93 | 53.03 | 52.36 | 52.55 | 52.30 | 53.15 | 53.28 | 53.78 | 53.46 |
| $TiO_2$ | 0.23 | 0.05 | 0.37 | 0.00 | 0.00 | 0.01 | 0.08 | 0.10 | 0.00 | 0.13 | 0.19 | 0.07 | 0.10 |
| $Al_2O_3$ | 0.51 | 0.79 | 1.12 | 0.89 | 0.83 | 0.86 | 0.66 | 0.29 | 0.48 | 0.71 | 0.51 | 0.34 | 0.21 |
| $Fe_2O_3$ | 2.79 | 0.21 | 1.20 | 0.00 | 0.00 | 1.69 | 3.06 | 0.00 | 0.07 | 3.13 | 2.06 | 0.58 | 1.01 |
| FeO | 5.48 | 15.82 | 5.93 | 17.16 | 18.78 | 7.44 | 5.67 | 22.73 | 22.46 | 5.31 | 6.08 | 21.44 | 20.70 |
| MnO | 0.43 | 1.03 | 0.39 | 0.63 | 0.71 | 0.45 | 0.54 | 1.05 | 1.00 | 0.36 | 0.33 | 1.03 | 0.92 |
| MgO | 16.14 | 23.75 | 15.32 | 28.32 | 27.01 | 14.74 | 14.86 | 22.10 | 22.10 | 15.47 | 15.02 | 23.01 | 23.26 |
| CaO | 19.85 | 1.77 | 21.44 | 0.31 | 0.28 | 21.37 | 22.03 | 1.13 | 1.04 | 22.14 | 22.38 | 0.60 | 0.62 |
| $Na_2O$ | 1.23 | 0.12 | 0.75 | 0.00 | 0.00 | 0.41 | 0.38 | 0.02 | 0.00 | 0.45 | 0.43 | 0.01 | 0.01 |
| $K_2O$ | 0.05 | 0.00 | 0.01 | 0.00 | 0.00 | 0.00 | 0.00 | 0.01 | 0.04 | 0.00 | 0.00 | 0.01 | 0.02 |
| Total | 99.47 | 98.78 | 99.88 | 100.24 | 101.55 | 100.02 | 99.63 | 99.98 | 99.50 | 100.94 | 100.41 | 100.88 | 100.32 |
| *Cations per formula unit* | | | | | | | | | | | | | |
| Si | 1.97 | 2.03 | 1.98 | 1.93 | 1.95 | 1.97 | 1.95 | 1.97 | 1.97 | 1.95 | 1.97 | 1.98 | 1.98 |
| Ti | 0.01 | 0.00 | 0.01 | 0.00 | 0.00 | 0.00 | 0.00 | 0.00 | 0.00 | 0.00 | 0.01 | 0.00 | 0.00 |
| Al | 0.02 | 0.03 | 0.05 | 0.04 | 0.04 | 0.04 | 0.03 | 0.01 | 0.02 | 0.03 | 0.02 | 0.01 | 0.01 |
| $Fe^{3+}$ | 0.08 | 0.01 | 0.03 | 0.00 | 0.00 | 0.05 | 0.09 | 0.00 | 0.00 | 0.09 | 0.06 | 0.02 | 0.03 |
| $Fe^{2+}$ | 0.17 | 0.49 | 0.18 | 0.52 | 0.57 | 0.23 | 0.18 | 0.71 | 0.71 | 0.16 | 0.19 | 0.66 | 0.64 |
| Mn | 0.01 | 0.03 | 0.01 | 0.02 | 0.02 | 0.01 | 0.02 | 0.03 | 0.03 | 0.01 | 0.01 | 0.03 | 0.03 |
| Mg | 0.90 | 1.30 | 0.85 | 1.54 | 1.45 | 0.82 | 0.83 | 1.24 | 1.24 | 0.85 | 0.83 | 1.27 | 1.28 |
| Ca | 0.80 | 0.07 | 0.85 | 0.01 | 0.01 | 0.85 | 0.88 | 0.05 | 0.04 | 0.87 | 0.89 | 0.02 | 0.02 |
| Na | 0.09 | 0.01 | 0.05 | 0.00 | 0.00 | 0.03 | 0.03 | 0.00 | 0.00 | 0.03 | 0.03 | 0.00 | 0.00 |
| K | 0.00 | 0.00 | 0.00 | 0.00 | 0.00 | 0.00 | 0.00 | 0.00 | 0.00 | 0.00 | 0.00 | 0.00 | 0.00 |
| *End members* | | | | | | | | | | | | | |
| Wollastonite | 0.40 | 0.04 | 0.42 | 0.01 | 0.01 | 0.41 | 0.43 | 0.02 | 0.02 | 0.42 | 0.44 | 0.01 | 0.01 |
| Enstatite | 0.45 | 0.65 | 0.42 | 0.77 | 0.73 | 0.41 | 0.41 | 0.62 | 0.62 | 0.42 | 0.41 | 0.63 | 0.64 |
| Ferrosilite | 0.09 | 0.24 | 0.09 | 0.26 | 0.28 | 0.12 | 0.09 | 0.36 | 0.35 | 0.08 | 0.09 | 0.33 | 0.32 |
| Pyroxmangit | 0.01 | 0.02 | 0.01 | 0.01 | 0.01 | 0.01 | 0.01 | 0.02 | 0.02 | 0.01 | 0.01 | 0.02 | 0.01 |

#### 4.2.2. Quartz

Quartz, in the form of partial melt films and pools in textural equilibrium with ilmenite, was only present in the barren charnockite (NM-57 drill core). Therefore, a systematic analysis on the variation of Ti concentration in quartz was conducted in this drill core. Analyses are summarized in Table 2.

**Table 2.** Titanium content (given in ppm) of the analyzed quartz crystals in the partial melts and calculated crystallization temperatures. Average error of the individual measurements is ±8%. (S = average of the individual Ti concentration measurements, given in ppm; σ = standard deviation of the titanium concentrations; $a_{Ti}$ = titanium activity in the quartz; $S_T$ (°C) = temperature calculated from the average Ti concentrations given in Celsius degree; σT (°C) = standard deviation of the temperature calculation, given in Celsius degree.

| **Sample Name** | **Z-151** | **Z-161** | | **Z-165** | **Z-169** |
|---|---|---|---|---|---|
| Depth (m) | 206 | 253 | | 296 | 319 |
| Petrographic position | Partial melt pool | Partial melt pool | Myrmekite | Myrmekite | Myrmekite |
| 1 | 360 | 151 | 205 | 161 | 161 |
| 2 | 360 | 174 | 190 | 189 | 189 |
| 3 | 409 | 159 | 204 | 173 | 173 |
| 4 | 350 | 164 | 150 | 176 | 176 |
| 5 | 370 | 151 | 142 | 184 | 181 |
| 6 | 360 | 189 | 135 | 176 | 200 |
| 7 | 410 | 141 | 143 | 168 | 176 |
| 8 | 360 | 63 | 134 | 129 | 168 |
| 9 | 422 | 206 | 184 | 170 | 127 |
| 10 | 260 | | 190 | 87 | 170 |
| 11 | 394 | | 166 | 100 | 199 |
| 12 | 404 | | 16.5 | 199 | 158 |
| 13 | | | 150 | 158 | 147 |
| 14 | | | 137 | 147 | 168 |
| 15 | | | 165 | 168 | 141 |
| 16 | | | | 141 | |
| 17 | | | | 81 | |
| S | 372 | 155 | 154 | 153 | 169 |
| σ | 43 | 38 | 28 | 29 | 18 |
| Min | 206 | 63 | 17 | 81 | 127 |
| Max | 422 | 206 | 205 | 199 | 200 |
| $a_{Ti}$ | 0.5 | 0.5 | 0.5 | 0.5 | 0.5 |
| $S_T$(°C) | 827.6 | 717.9 | 716.9 | 716.4 | 727.4 |
| σT(°C) | 17.4 | 36.0 | 56.0 | 29.0 | 14.0 |

The highest values in a sample 5 m beneath the contact, ranged from 260–420 ppm; the median of 12 measurements was 372 ppm. In the most distant sample, Ti in the myrmekitic quartz ranged from 127 to 200 ppm and the median of 15 analyses was 169 ppm.

#### 4.2.3. Biotite

Representative compositions of biotite II (euhedral, rosette-like) are listed in Table 3, and the classification of the biotite II compositions, based on their $^{IV}$Al (atomic proportion per formula unit (apfu)) and Mg# (=Mg/(Mg + $Fe^{2+}$) atom proportion) content, are plotted in Figure 5. Structural formulae are calculated on the basis of 12 (O, OH, F, Cl) apfu. Composition of biotite II in the charnockite shows very little variation. All samples fall in the phlogopite field (ideal formula: $KMg_3$ $(Si_3Al)O_{10}(OH,F)_2$). The composition of the biotite in the metapelite had a larger variation and had higher annite content [$KFe^{2+}{}_3(Si_3Al)O_{10}(OH,F)_2$]

**Table 3.** Representative electron microprobe analyses of biotite compositions.

| **Deposit** | **Serpentine** | | | | **Dunka Pit** | | | | **Spruce Road** | | | |
|---|---|---|---|---|---|---|---|---|---|---|---|---|
| Drill hole | B1-178 | B1-178 | B1-178 | B1-178 | NM-57 | NM-57 | NM-57 | NM-57 | WM-002 | WM-002 | WM-002 | WM-002 |
| Depth (m) | 132.7 | 132.7 | 167.2 | 167.2 | 253.1 | 253.1 | 306.3 | 302.0 | 195.4 | 195.4 | 257.9 | 257.9 |
| Sample | Z-118 | Z-118 | Z-118 | Z-118 | Z-161 | Z-161 | Z-168 | Z-167 | Z2-28 | Z2-28 | Z2-54 | Z2-54 |
| Mineral | *bt* | *bt* | *bt* | *bt* | *bt* | *bt* | *bt* | *bt* | *bt* | *bt* | *bt* | *bt* |
| *wt%* | | | | | | | | | | | | |
| $SiO_2$ | 35.11 | 35.48 | 37.04 | 38.15 | 38.24 | 37.77 | 37.80 | 38.12 | 38.96 | 38.28 | 37.37 | 37.35 |
| $TiO_2$ | 3.79 | 3.80 | 5.03 | 4.75 | 4.62 | 4.54 | 4.59 | 4.73 | 2.89 | 3.75 | 5.07 | 4.84 |
| $Al_2O_3$ | 16.37 | 16.80 | 14.16 | 14.23 | 14.44 | 15.19 | 14.21 | 14.63 | 13.12 | 12.55 | 12.86 | 12.72 |
| $Cr_2O_3$ | 0.13 | 0.12 | 0.41 | 0.38 | 0.00 | 0.00 | 0.00 | 0.00 | 0.00 | 0.00 | 0.00 | 0.00 |
| FeO | 23.57 | 23.49 | 17.37 | 16.19 | 14.65 | 17.13 | 13.67 | 13.47 | 15.14 | 15.59 | 13.61 | 13.92 |
| MnO | 0.11 | 0.05 | 0.02 | 0.03 | 0.00 | 0.44 | 0.32 | 0.26 | 0.32 | 0.39 | 0.20 | 0.18 |
| MgO | 7.79 | 7.66 | 12.32 | 12.75 | 13.99 | 12.34 | 14.36 | 14.03 | 15.55 | 15.59 | 15.16 | 15.55 |
| CaO | 0.04 | 0.00 | 0.00 | 0.10 | 0.00 | 0.00 | 0.00 | 0.00 | 0.10 | 0.05 | 0.00 | 0.00 |
| $Na_2O$ | 0.13 | 0.10 | 0.04 | 0.02 | 0.00 | 0.10 | 0.06 | 0.10 | 0.06 | 0.11 | 0.19 | 0.14 |
| $K_2O$ | 9.33 | 9.16 | 9.70 | 9.93 | 10.16 | 9.99 | 9.94 | 10.03 | 9.41 | 9.69 | 9.53 | 9.62 |
| F | 0.37 | 0.41 | 0.57 | 0.60 | 0.79 | 0.77 | 1.28 | 1.34 | 0.36 | 0.34 | 0.54 | 0.55 |
| Cl | 0.08 | 0.08 | 0.05 | 0.02 | 0.06 | 0.11 | 0.00 | 0.00 | 0.04 | 0.03 | 0.26 | 0.27 |
| $H_2O$ | 3.61 | 3.62 | 3.61 | 3.64 | 3.57 | 3.57 | 3.31 | 3.31 | 3.79 | 3.79 | 3.59 | 3.63 |
| Subtotal | 100.44 | 100.76 | 100.31 | 100.81 | 100.53 | 101.95 | 99.56 | 100.01 | 99.74 | 100.16 | 99.61 | 100.53 |
| F,Cl=O | 0.17 | 0.19 | 0.25 | 0.26 | 0.35 | 0.35 | 0.54 | 0.57 | 0.16 | 0.15 | 0.29 | 0.29 |
| Total | 100.27 | 100.57 | 100.06 | 100.55 | 100.18 | 101.61 | 99.02 | 99.45 | 99.58 | 100.01 | 99.33 | 100.23 |
| *Calculated formula based on 12 (O,OH,F,Cl)* | | | | | | | | | | | | |
| Si | 2.77 | 2.77 | 2.86 | 2.91 | 2.90 | 2.86 | 2.89 | 2.90 | 2.94 | 2.90 | 2.86 | 2.83 |
| Ti | 0.22 | 0.22 | 0.29 | 0.27 | 0.26 | 0.26 | 0.26 | 0.27 | 0.16 | 0.21 | 0.29 | 0.28 |
| Al | 1.52 | 1.55 | 1.29 | 1.28 | 1.29 | 1.35 | 1.28 | 1.31 | 1.17 | 1.12 | 1.16 | 1.14 |
| Cr | 0.01 | 0.01 | 0.02 | 0.02 | 0.00 | 0.00 | 0.00 | 0.00 | 0.00 | 0.00 | 0.00 | 0.00 |
| $Fe^{2+}$ | 1.55 | 1.54 | 1.12 | 1.03 | 0.93 | 1.08 | 0.87 | 0.86 | 0.96 | 0.99 | 0.87 | 0.88 |
| Mn | 0.01 | 0.00 | 0.00 | 0.00 | 0.00 | 0.03 | 0.02 | 0.02 | 0.02 | 0.03 | 0.01 | 0.01 |
| Mg | 0.91 | 0.89 | 1.42 | 1.45 | 1.58 | 1.39 | 1.64 | 1.59 | 1.75 | 1.76 | 1.73 | 1.76 |
| Ca | 0.00 | 0.00 | 0.00 | 0.01 | 0.00 | 0.00 | 0.00 | 0.00 | 0.01 | 0.00 | 0.00 | 0.00 |

**Table 3.** *Cont.*

| **Deposit** | **Serpentine** | | | | **Dunka Pit** | | | | **Spruce Road** | | | |
|---|---|---|---|---|---|---|---|---|---|---|---|---|
| Na | 0.02 | 0.01 | 0.01 | 0.00 | 0.00 | 0.01 | 0.01 | 0.01 | 0.01 | 0.02 | 0.03 | 0.02 |
| K | 0.94 | 0.91 | 0.95 | 0.97 | 0.98 | 0.96 | 0.97 | 0.97 | 0.91 | 0.94 | 0.93 | 0.93 |
| F | 0.09 | 0.10 | 0.14 | 0.15 | 0.19 | 0.18 | 0.31 | 0.32 | 0.09 | 0.08 | 0.13 | 0.13 |
| Cl | 0.01 | 0.01 | 0.01 | 0.00 | 0.01 | 0.01 | 0.00 | 0.00 | 0.00 | 0.00 | 0.03 | 0.03 |
| H | 1.90 | 1.89 | 1.86 | 1.85 | 1.80 | 1.80 | 1.69 | 1.68 | 1.91 | 1.92 | 1.84 | 1.83 |
| Mg# ($Fe_{tot}$) | 0.37 | 0.37 | 0.56 | 0.58 | 0.63 | 0.56 | 0.65 | 0.65 | 0.65 | 0.64 | 0.67 | 0.67 |
| Al (IV) | 1.23 | 1.23 | 1.14 | 1.09 | 1.10 | 1.14 | 1.11 | 1.10 | 1.06 | 1.10 | 1.14 | 1.14 |
| Al (VI) | 0.29 | 0.32 | 0.15 | 0.19 | 0.19 | 0.21 | 0.17 | 0.21 | 0.11 | 0.02 | 0.02 | 0.00 |
| # Cations | 7.96 | 7.92 | 7.96 | 7.94 | 7.95 | 7.95 | 7.95 | 7.93 | 7.92 | 7.96 | 7.96 | 7.95 |

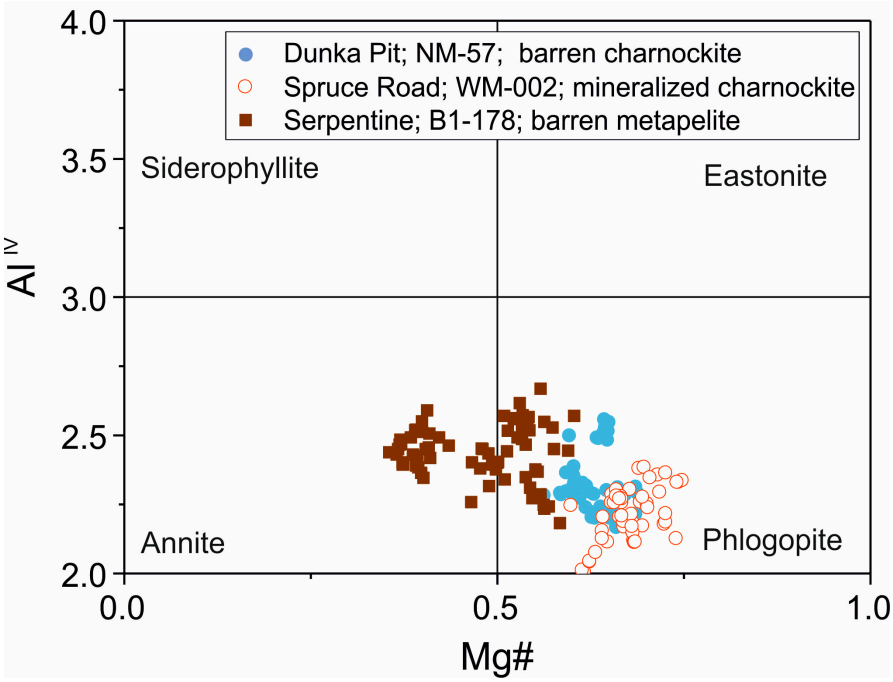



**Figure 5.** Classification of euhedral and subhedral biotite crystals that formed during the contact metamorphism based on Mg# and $^{IV}$Al content (on an apfu basis).

Magnesium numbers (Mg#) in the metapelite (B1-178 drill core) and in the mineralized charnockite (WM-002 drill core) increase from 0.35 to 0.63 atoms per formula unit (apfu) and from 0.66 to 0.77 apfu, respectively, with increasing distance from the intrusion/footwall contact. In the barren charnockite (NM-57 drill core), the Mg# does not show any systematic variation with depth (0.57–0.68) (Figure 6a). The F content increased with increasing depth in the metapelite and in the mineralized charnockite from 0.07 to 0.15 and from 0.02 to 0.19, respectively, but decreases with the distance from the footwall/intrusion contact in the barren charnockite from 0.3 to 0.09 apfu (Figure 6b). Chlorine content in biotite from the metapelite was very low (<0.025 apfu) and displayed little variation with distance from the contact. Chlorine in biotite II in the barren charnockitic samples was always below the detection limit (0.1 wt. %). Chlorine content of biotite II in the mineralized charnockite varied between 0 and 0.05 apfu and displayed an increasing trend with depth.

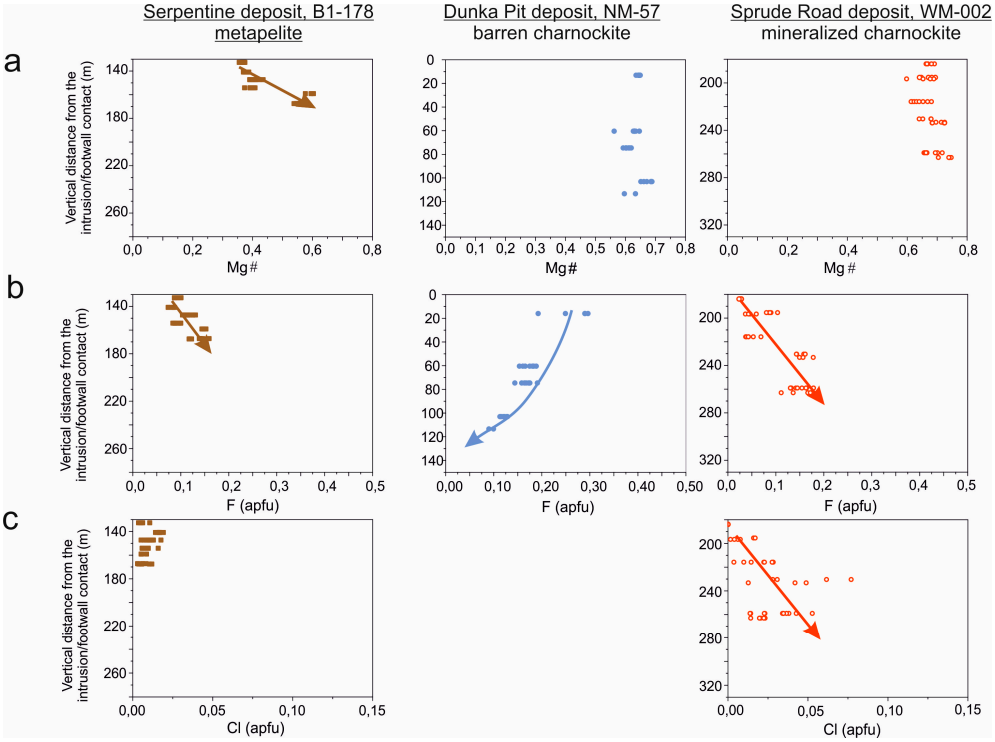



**Figure 6.** (**a**) Depth versus Mg# of biotite diagrams of the footwall of the studied drill cores. The top of the plots coincides with the intrusion-footwall contact. The Mg# in biotite is increasing with increasing depth in the B1-178 and WM-002 drill cores but does not vary in the barren NM-57 drill core. (**b**) Depth versus F (on the basis of apfu) diagrams of the studied drill cores. Fluorine content of biotite increased with increasing depth at the Serpentine and Spruce Road deposits but decreased at the Dunka Pit deposit. (**c**) Depth versus Cl (on the basis of apfu) in the analyzed biotite crystals. Note the significant increase of Cl content of biotite in the mineralized WM-002 drill core at the Spruce Road deposit. Cl content of biotite at the Dunka Pit deposit is below detection limit (0.1 wt. %) and is not presented in the figure.

#### 4.2.4. Apatite

In order to trace variation in the activity of chlorine in the syn-metamorphic fluids, apatite crystals in textural equilibrium with euhedral biotite II crystals or in equilibrium with partial melts were selected for analysis. Representative apatite compositions are listed in Table 4 and plotted in Figure 6.

The chlorine content in apatite from the metapelite was low (0.02–0.05 apfu) and the Cl/F (atomic ratio) varied between 0 and 0.05. The abundance of Cl in the barren charnockite shows a decreasing trend with depth (0.15 to 0.05 apfu), whereas the F content is rather constant (1.27–1.85 apfu). Therefore, the Cl/F atomic ratio decreases with increasing distance from the footwall-intrusion contact. In the mineralized charnockite, the abundance of F does not show variation (0.36–0.8 apfu), whereas the Cl content increase (from 0.03 to 0.39 apfu) with increasing depth. Accordingly, the Cl/F ratio increase with depth in the footwall. Independently of the Cl/F variations, in each samples the apatite has fluor-apatite composition (Figure 7a).

For comparison, apatite in the Giants Range batholith, far from the intrusion (~15 km), was also analyzed. Apatite in the footwall granite is F-rich (0.9 apfu) with Cl content below the detection limit (Figure 7a).

**Table 4.** Representative electron microprobe analyses of apatite compositions.

| **Deposit** | **Giants Range Batholite** | | **Serpentine** | | | | **Dunka Pit** | | | | **Spruce Road** | | | |
|---|---|---|---|---|---|---|---|---|---|---|---|---|---|---|
| Drill hole | | | B1-178 | B1-178 | B1-178 | B1-178 | NM-57 | NM-57 | NM-57 | NM-57 | WM-002 | WM-002 | WM-002 | WM-002 |
| Depth (m) | | | 132.7 | 132.7 | 167.2 | 167.2 | 253.4 | 253.4 | 306.3 | 302.0 | 192.0 | 192.0 | 293.5 | 293.5 |
| Sample | | | Z-118 | Z-118 | Z-131 | Z-131 | Z-161 | Z-161 | Z-165 | Z-165 | Z2-26 | Z2-26 | Z2-60 | Z2-60 |
| Mineral | | | ap | ap | ap | ap | ap | ap | ap | ap | ap | ap | ap | ap |
| *wt%* | | | | | | | | | | | | | | |
| $SiO_2$ | 0.22 | 0.07 | 0.00 | 0.05 | 0.00 | 0.09 | 0.38 | 0.03 | 0.50 | 0.36 | 0.19 | 0.26 | 0.05 | 0.26 |
| $Al_2O_3$ | 0.02 | 0.00 | 0.11 | 0.15 | 0.09 | 0.24 | 0.08 | 0.16 | 0.18 | 0.00 | 0.18 | 0.02 | 0.13 | 0.06 |
| $P_2O_5$ | 41.63 | 41.62 | 41.77 | 41.60 | 41.89 | 41.89 | 41.05 | 41.85 | 40.85 | 41.02 | 42.70 | 43.00 | 40.82 | 40.36 |
| FeO | 0.00 | 0.00 | 1.39 | 0.85 | 0.17 | 0.10 | 0.33 | 0.00 | 0.09 | 0.13 | 0.21 | 0.26 | 0.00 | 0.06 |
| MgO | 0.00 | 0.00 | 0.42 | 0.25 | 0.00 | 0.00 | 0.05 | 0.08 | 0.00 | 0.00 | 0.00 | 0.00 | 0.04 | 0.04 |
| CaO | 55.65 | 55.48 | 52.66 | 53.37 | 54.21 | 54.18 | 55.01 | 54.86 | 54.15 | 54.65 | 51.98 | 52.71 | 54.26 | 54.25 |
| $K_2O$ | 0.00 | 0.00 | 0.34 | 0.37 | 0.03 | 0.00 | 0.00 | 0.00 | 0.00 | 0.00 | 0.00 | 0.00 | 0.00 | 0.00 |
| F | 3.48 | 3.31 | 2.99 | 3.25 | 2.67 | 2.45 | 3.53 | 3.38 | 2.50 | 2.75 | 2.57 | 2.89 | 2.18 | 2.04 |
| Cl | 0.00 | 0.00 | 0.15 | 0.11 | 0.35 | 0.31 | 0.16 | 0.20 | 0.28 | 0.27 | 0.26 | 0.38 | 1.27 | 1.27 |
| $H_2O$ | 0.05 | 0.10 | 0.27 | 0.17 | 0.39 | 0.50 | 0.05 | 0.11 | 0.48 | 0.38 | 0.39 | 0.23 | 0.39 | 0.46 |
| Total | 101.05 | 100.58 | 100.09 | 100.18 | 99.80 | 99.76 | 100.78 | 100.68 | 99.02 | 99.61 | 98.47 | 99.75 | 99.25 | 99.10 |
| F,Cl=O | 1.28 | 1.62 | 1.29 | 1.39 | 1.20 | 1.10 | 1.52 | 1.47 | 1.12 | 1.22 | 1.14 | 1.30 | 1.21 | 1.14 |
| *Cation numbers based on 26 (O, OH, F, Cl)* | | | | | | | | | | | | | | |
| Si | 0.00 | 0.00 | 0.00 | 0.01 | 0.00 | 0.02 | 0.06 | 0.01 | 0.09 | 0.06 | 0.03 | 0.05 | 0.01 | 0.04 |
| Al | 0.00 | 0.00 | 0.02 | 0.03 | 0.02 | 0.05 | 0.02 | 0.03 | 0.04 | 0.00 | 0.04 | 0.00 | 0.03 | 0.01 |
| P | 5.75 | 5.61 | 6.15 | 6.07 | 6.10 | 6.11 | 5.89 | 6.02 | 5.96 | 5.93 | 6.49 | 6.45 | 5.94 | 5.87 |
| $Fe^{2+}$ | 0.00 | 0.00 | 0.20 | 0.12 | 0.02 | 0.01 | 0.05 | 0.00 | 0.01 | 0.02 | 0.03 | 0.04 | 0.00 | 0.01 |
| Mg | 0.00 | 0.00 | 0.11 | 0.06 | 0.00 | 0.00 | 0.01 | 0.02 | 0.00 | 0.00 | 0.00 | 0.00 | 0.01 | 0.01 |
| Ca | 9.73 | 9.66 | 9.82 | 9.86 | 9.99 | 10.00 | 9.99 | 9.98 | 10.00 | 10.00 | 10.00 | 10.00 | 9.99 | 9.99 |
| K | 0.00 | 0.00 | 0.07 | 0.08 | 0.01 | 0.00 | 0.00 | 0.00 | 0.00 | 0.00 | 0.00 | 0.00 | 0.00 | 0.00 |
| F | 1.79 | 2.07 | 1.64 | 1.77 | 1.45 | 1.33 | 1.89 | 1.81 | 1.36 | 1.49 | 0.46 | 1.62 | 1.19 | 1.11 |
| Cl | 0.00 | 0.01 | 0.04 | 0.03 | 0.10 | 0.09 | 0.05 | 0.06 | 0.08 | 0.08 | 0.08 | 0.11 | 0.37 | 0.37 |
| H | 0.20 | 0.26 | 0.31 | 0.20 | 0.45 | 0.58 | 0.06 | 0.13 | 0.55 | 0.43 | 0.46 | 0.27 | 0.44 | 0.52 |
| $X^{OH}$ | 0.10 | 0.14 | 0.16 | 0.10 | 0.22 | 0.29 | 0.03 | 0.06 | 0.28 | 0.22 | 0.23 | 0.13 | 0.22 | 0.26 |
| $X^{F}$ | 0.90 | 0.86 | 0.82 | 0.89 | 0.73 | 0.67 | 0.95 | 0.91 | 0.68 | 0.74 | 0.73 | 0.81 | 0.59 | 0.55 |
| $X^{Cl}$ | 0.00 | 0.00 | 0.02 | 0.02 | 0.05 | 0.05 | 0.02 | 0.03 | 0.04 | 0.04 | 0.04 | 0.06 | 0.19 | 0.19 |

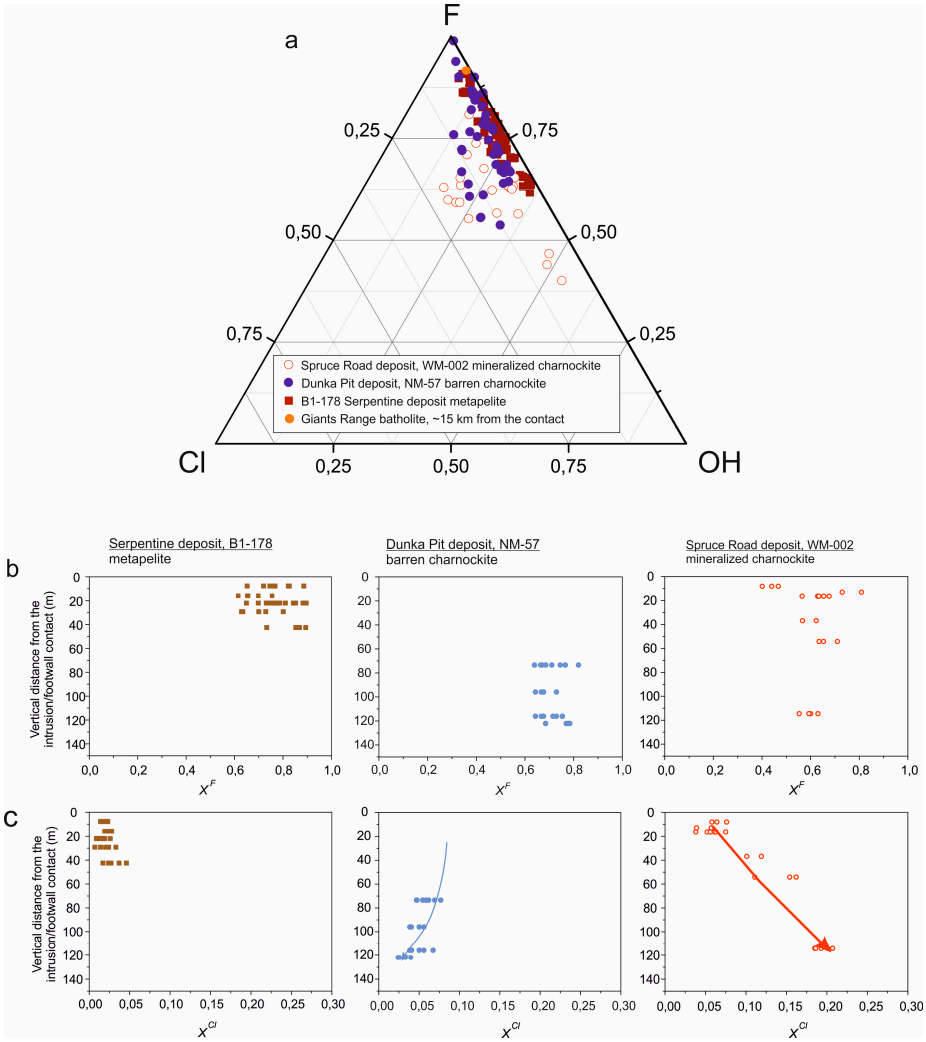



**Figure 7.** (**a**) Composition of apatite. (**b**,**c**) Depth versus mole fractions of Cl ($X^{Cl}$) and F ($X^F$) in apatite in the footwall of the studied drill cores. The top of the plots coincided with the intrusion-footwall contact. Note the two opposite trends: $X^{Cl}$ in the Serpentine and Spruce Road deposits increased with increasing depth, whereas it decreased in the Dunka Pit deposit in the NM-57 drill core.

### *4.3. Two-Pyroxene, Titanium-in-Quartz, and Biotite-Apatite Thermometry*

The two-pyroxene thermometer was primarily developed for magmatic rocks [26] and it has several problems when applied to metamorphic rocks, primarily in granulites [46]. Nevertheless, meaningful data from the Agto granulite (West Greenland) were previously reported [47]. Compositions of enstatite and augite in textural equilibrium at the Spruce Road deposit indicate 900–1000 °C temperature up to 15 m from the intrusion-footwall contact and 700–750 °C temperature in the distal part of the contact aureole (up to 97 m from the intrusion-footwall contact). A systematic variation of temperature with depth was also observed in the barren charnockite. At 68 and 107 m below the intrusion-footwall contact the temperature was around 800 °C and 700 °C, respectively. Temperatures obtained with the two-pyroxene thermometers fit well to the previous temperature estimations [47]. As it is presented below, other thermometers confirmed the applicability of this method in the studied sections.

The theoretical and practical background of the Titanium-in-quartz thermometer has been published previously [27] and successfully applied to magmatic and metamorphic conditions. Applicability of the Ti-in-quartz thermometer for partially molten pelitic rocks was presented previously [48]. Ti content of quartz in Ti-saturated systems (in the presence of Ti bearing mineral phases,

e.g., rutile, titanite) varied systematically with the formation temperature of the quartz crystal. Temperatures were calculated using the equation

$$T(^{\circ}\mathrm{C}) = \frac{-3765}{\log\left(\frac{X_{Ti}^{qtz}}{a_{TiO2}}\right) - 5.69} - 273, \quad (1)$$

where $X_{Ti}^{qtz}$ is the Ti concentration in quartz and $a_{TiO_2}$ is the activity of $TiO_2$ of the system. In the presence of rutile, $a_{TiO2}$ is 1. In rocks where rutile is absent, but other Ti-bearing minerals like ilmenite or titanite are present, $a_{TiO_2}$ will vary between 0 and 1. According to studies [26], in silicic igneous rocks, activity of 0.5 or higher is seen to be relevant. Purity (inclusions) and homogeneity (lack of growth zonation) of the analyzed quartz was checked by SEM and SEM-CL.

The results of the Titanium-in-quartz geothermometer (Table 2) agreed with the two-pyroxene thermometry estimations in the barren charnockite. However, slight temperature differences were detected between symplectitic quartz and melt pools where the calculated data overlap was within one sigma error. The crystallization temperature was around 825 ± 17 °C for the quartz in a partial melt pool up to 7 m from the intrusion-footwall contact in the mineralized drill core, and temperatures up to 727 ± 14 °C in the barren drill core reinforced that the maximum temperatures were lower in the barren drill core.

Apatite and biotite grains in the metapelite, barren, and mineralized charnockite that were in direct contact were selected for biotite-apatite thermometry, and hence their equilibrium was assumed during their crystallization (Figure 3a–c). This thermometer had been used successfully for many types of high temperature magmatic-metamorphic-hydrothermal systems [28,49–51], because apatite is less prone to low temperature subsolidus re-equilibration than silicates. The temperatures were calculated using the equation [28]:

$$T(^{\circ}\mathrm{C}) = \left((8852 - 0.024P(bars) + 5000X_{Fe}^{Bi})/(1.987lnK_d^{\frac{Ap}{Bi}} + 3.3666)\right) - 273.15 \quad (2)$$

where $X_{Fe}^{Bi} = (Fe^{2+} + Al^{VI})(Fe^{2+} + Mg + Al^{VI})$; and $K_d^{Ap/Bi} = \left(\frac{X^F}{X^{OH}}\right)^{Ap} / \left(\frac{X^F}{X^{OH}}\right)^{Bi}$.

$X^F$ and $X^{OH}$ are mole fractions of F and OH in apatite and biotite. The pressure was set to 1.8 kbar according to pressure estimations [9,38] based on fluid inclusion studies. The largest error in the estimates is due to the analysis of F measurements, especially if the concentration of the fluorine is close to the detection limit of the WDX.

In the barren charnockite, the results of the biotite-apatite geothermometer showed remarkable agreement with the results of the two-pyroxene and titanium in quartz thermometers (Figure 8). Close to the contact (up to 10 m) the temperatures exceeded 800 °C. With increasing depth, the decrease of the temperature gradient became modest and the temperature decreased to around 650 °C at 120 m from the intrusion-footwall contact. In the metapelite, only a short segment was analyzed but the temperatures were comparable with the barren charnockite—the temperature decreased from 800° to around 700 °C beneath the contact (Figure 8).

In the mineralized drill core, there was a significant difference in the temperatures estimated by the two-pyroxene and the apatite-biotite thermometer (Figure 8). The apatite-biotite thermometer provided temperatures (600–720 °C) that were around 200 °C lower than those obtained with the two-pyroxene thermometer and estimated earlier [16]. The difference could be the result of: (1) two-pyroxene thermometer was not calibrated for high temperature contact metamorphic processes and hence its applicability is questionable, (2) even if the most idiomorphic pyroxene crystals were selected for analysis, incomplete alteration of biotite I to pyroxene or retrogression of pyroxene to biotite or amphibole may affect the equilibrium compositions, (3) the two-pyroxene thermometer represents the peak metamorphic temperature, whereas the biotite-apatite thermometer infers retrograde metamorphic temperatures postdating the peak metamorphic temperatures, (4) multiple processes:

e.g., the mineralized zones were the sites of magma channels thus several pulses of magma were driven there causing variation in temperature and slower cooling compared to the barren zones which were upheated once and then cooled monotonously.

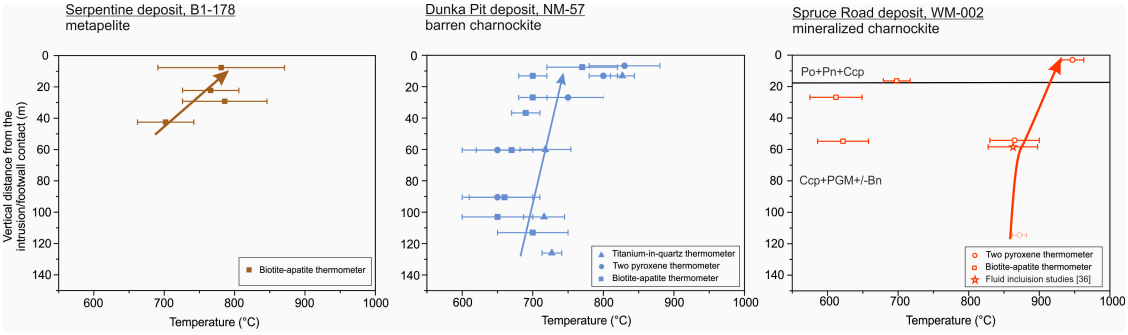



**Figure 8.** Variation of temperature in the footwall of the studied drill cores using titanium-in-quartz, two-pyroxene, and biotite-apatite thermometers. The top of the plots coincides with the intrusion-footwall contact.

## 5. Discussion

### *5.1. Petrographic Evidence and Evaluation of the Temporal-Spatial Extent of the Partial Melting*

Several petrographic and textural differences exist between the studied barren (Dunka Pit, NM-57 drill core) charnockitic and metapelitic rocks and the mineralized (Spruce Road, WM-002 drill core) charnockitic rocks. Textural signs of partial melting, including partial melt films, pools, partial melt pockets, and symplectitic intergrowths between quartz and feldspars, are abundant up to 100 m from the intrusion-footwall contact in the mineralized drill cores. Although local segregation of leucosome and melanosome is observed in the barren charnockite up to 30 m from the intrusion-footwall contact, textural evidence of partial melting diminishes with increasing depth to finally disappear 100 m from the contact. Another striking difference is in the mafic mineral assemblage. In the mineralized charnockite, pyroxene crystals are euhedral and free of resorbed biotite I or hornblende crystals. Contrarily, in the barren charnockite, pyroxene crystals, rich in resorbed biotite I, indicate that metamorphic reactions were not complete. This can be explained by: (1) the different fugacity of fluids during the contact metamorphism, i.e., the fluids acted as catalysts of mineral reactions in the mineralized drill core and/or (2) the rock did not remain hot enough and metamorphic mineral reactions were incomplete.

### *5.2. Evaluation of Temperature During Partial Melting*

The peak temperature of the contact metamorphism can be estimated semi-quantitatively on the basis of experimental studies if the parent rock composition is known. The South Kawishiwi intrusion at the Birch Lake area is in contact with hornblende-adamellite-granodiorite [36]. According to previous studies [16,52], the orthopyroxene, clinopyroxene, and melt could have formed during the following model reaction:

$$\begin{array}{c}\text{hornblende + biotite + quartz + orthoclase + Ab from plagioclase =}\\ \text{clinopyroxene + orthopyroxene + plagioclase + magnetite + melt}\end{array} \quad (3)$$

Experimental studies on meta-greywackes in the pressure range between 1 to 3 kbar indicated that the breakdown of biotite starts between 800 and 925 °C [53–55]. Hornblende breakdown in most intermediate composition amphibolites below 5 kbar is initiated at 850 °C [53]. Thus, comparing results of petrographic observations and experimental studies cited above, co-existing orthopyroxene + clinopyroxene + plagioclase + magnetite + melt (that further crystallized to quartz + K-feldspar +

plagioclase), as well as the corroded biotite I, indicate the minimum temperature of charnockitization was above 800 °C.

Experimental studies on the stability relationships of ferromagnesian mineral assemblages in synthetic granitic compositions at 2 kbar pressure [25] are comparable with the pressures around 1.6–2 kbar in the footwall of the South Kawishiwi intrusion [38]. Also, the chemical and modal compositions of the granite in the experiments are comparable with the parent rock compositions of the Giants Range batholith (Table 5).

**Table 5.** Comparison of chemical composition (given in wt%) of the Giants Range batholith and synthetic granites used in the experimental studies [25].

| | **Giants Range Batholith** | | **Synthetic Granite Compositions [25]** | |
|---|---|---|---|---|
| ***wt%*** | ***Granite (Embarrass)*** | ***Hornblende-biotite granite*** | | |
| $SiO_2$ | 72.39 | 66.31 | 70.77 | 67.51 |
| $TiO_2$ | 0.49 | 0.49 | - | - |
| $Al_2O_3$ | 13.39 | 12.70 | 14.83 | 17.45 |
| $Fe_2O_3$ | 0.18 | 1.98 | 2.44 | 2.44 |
| FeO | 1.44 | 2.66 | - | - |
| MnO | 0.01 | 0.04 | - | - |
| MgO | 1.61 | 3.01 | 1.19 | 1.19 |
| CaO | 0.92 | 4.77 | 1.34 | 3.52 |
| $Na_2O$ | 5.35 | 5.03 | 3.33 | 3.90 |
| $K_2O$ | 2.42 | 2.33 | 6.10 | 3.99 |
| $P_2O_5$ | 0.10 | 0.13 | - | - |
| $ZrO_2$ | 0.15 | 0.13 | - | - |

Experimental studies show that orthopyroxene, clinopyroxene, plagioclase, ± biotite, and melt are in equilibrium in water undersaturated conditions (<4 wt. % $H_2O$) between 800 and 850 °C [24]. The stability field of biotite + clinopyroxene + orthopyroxene + plagioclase + K-feldspar + melt assemblage ranges from 740 to 820 °C (Figure 9).

In line with previous experimental studies [52–55], the observed mineral assemblage (orthopyroxene + clinopyroxene + (resorbed) biotite I + plagioclase + partial melt) in the mineralized charnockite indicates that the mineral assemblage formed between 800 to 850 °C and that the system was vapor undersaturated (<4 wt. % $H_2O$). The lack of biotite in some samples or the presence of resorbed biotite I indicate that the temperature could be slightly higher but low vapor saturation or the duration of the peak metamorphic conditions hindered the complete biotite breakdown reactions. Biotite I is partially replaced by orthopyroxene in the barren charnockite. This feature, together with the occurrence of K-feldspar, indicate slightly lower temperatures (740–820 °C) in the unmineralized charnockite.

The two-pyroxene and titanium-in-quartz thermometers also support the temperature variations deduced from the mineral parageneses (Figure 9). In the barren charnockite the maximum temperatures were around 800 °C, whereas in the mineralized charnockite the temperature exceeded 900 °C during the contact metamorphism. Results of previous fluid inclusion studies [39] further support the high (810–920 °C) peak metamorphic conditions in the mineralized charnockite.

The temperature values obtained by the two-pyroxene thermometry and by the apatite-biotite thermometry are significantly different in the mineralized charnokite of the WM-002 drill core. The occurrence of biotite II close to the contact suggests that biotite may have had formed as a result of the following melt-back reaction:

$$\text{orthopyroxene + K-feldspar + melt = biotite + quartz} \quad (4)$$

Therefore, the temperature obtained by means of the apatite-biotite thermometer represents the early-retrograde phase of the contact metamorphism, when fluids re-entered into the dehydrated

charnockitic footwall, and not the earlier peak metamorphic conditions marked by synchronous formation of ortho- and clinopyroxene.

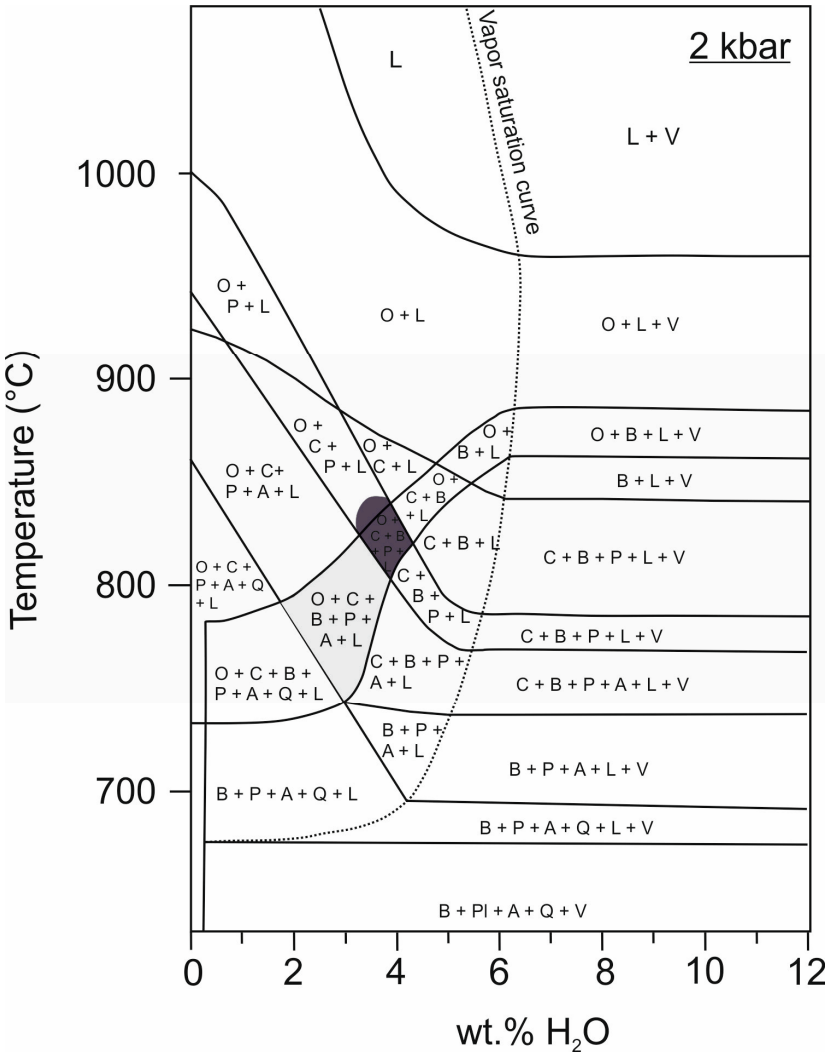



**Figure 9.** Mineral assemblages in the NM-57 drill core (light grey) and WM-002 drill cores (dark grey) projected on the temperature versus wt. percent $H_2O$ phase assemblage diagram for synthetic granite compositions [25]. (L = liquid, V = vapor, O = orthopyroxene, C = clinopyroxene, B = biotite, P = plagioclase, Q = quartz, A = alkali feldspar).

Based on the above considerations, two major differences can be recognized regarding the temperatures in barren and mineralized footwall zones. Firstly, the temperature adjacent to the intrusion-footwall contact was higher by around 100 °C at the Spruce Road deposit in the mineralized footwall (WM-002 drill core) compared to the barren footwall at the contact in the Dunka Pit deposit. Secondly, the abundant occurrence of partial melt pocket and biotite-bearing leucosome up to 100 m from the contact indicate a spatially more extended partial melting process, i.e., persistent high temperatures even far from the intrusion-footwall contact at the Spruce Road deposit. Conversely, in the barren charnockite and in the barren metapelite, rare petrographic evidence of partial melting (quartz-plagioclase symplectite, partial melt films) and the presence of inclusion-rich pyroxene all suggest that the metamorphic reactions remained incomplete.

The temperature differences between the mineralized and barren footwall zones can be best explained adopting the magma conduit model [1,12,13]. Based on this model, we suggest that beyond the mineralized footwall at the Spruce Road deposit a magma conduit existed with streaming,

sulfide-rich magma. The continuous magma replenishment in the magma conduit may have maintained the high temperature in the footwall for an extended time period. Persistent or cyclic reheating of the footwall supported the partial melting and hence the formation of a "permeable" rock volume. Sulfide liquid may have penetrated into the footwall using this permeability, even 100 m from the basal contact of the intrusion.

In contrast, at the Dunka Pit and Serpentine deposits, where the footwall remained barren, probably no magma conduit was present at the bottom of the intrusion. Therefore, the time interval when the footwall was continuously in contact with hot magma was much shorter, and this impeded the formation of a broad, partially-molten permeable zone.

It should also be considered that the temperature of the sulfide melt segregated from the parent intrusion was certainly at least 1100 °C. Cooling below 1100 °C generated precipitation of the mono-sulfide solid solution with low Pd/Rh ratios and enrichment of Cu, Pd, and Pt in the residual sulfide melt. Crystallization of the copper-rich intermediate sulfide solution phase, characterized by higher Pd/Rh ratios, begins at around 900 °C. Thus, mobility of sulfide droplets and residua sulfide liquids is possible at around and above 900 °C, but it is less probable as conditions cools below 900 °C [56]. This is in a good agreement with restriction of mineralization to those zones of the footwall, where the temperature reached or was exceeded 900 °C. In the mineralized charnockite at the Spruce Road deposit, the above delineated compositional evolution of the sulfide liquid was observed [22]. In the proximal zones, the sulfide liquid crystallized to pyrrhotite + pentrlandite + chalcopyrite, and with increasing distance, mainly chalcopyrite (+PGM) crystallized from the low temperature and low viscosity sulfide liquid.

Sulfide compositional variations in relation to sulfide liquid evolution and decreasing temperatures in mafic igneous complexes have been shown at other localities, such as Noril'sk [57] and Sudbury [11,58,59]. Infiltration of sulfide into partially molten footwall rocks was observed at the Bushveld complex [11].

However, it has to be noted that bornite, observed in the distal part of the mineralized WM-002 drill core, cannot crystallize from sulfide liquid [60–62]. Therefore, the presence of bornite is likely the result of mineral replacement reactions from the primary sulfides (mainly chalpoyrite), due to fluid alteration at lower temperatures [63].

### *5.3. Variation of $Log(f_{HF}/f_{HCl})_{fluid}$ and $Log(f_{H2O}/f_{HF})_{fluid}$ of Metamorphic Fluids in the Footwall Based on Halogen Concentrations of Biotite*

Nevertheless, the experiments referred to above do not involve the effect of F, Cl, and other halogen elements that may dramatically influence the onset of breakdown reactions. The deduced temperature ranges are only rough estimations, and the effect of the halogens will be discussed later in this paper.

Several lines of evidence presented above, including formation of clino- and orthopyroxene, and almost pure $CO_2$ fluid inclusions in syn-metamorphic quartz [39], show that during the peak of the metamorphism the system was $H_2O$ undersaturated. However, euhedral biotite II replacing the orthopyroxene indicates that subsequent to the formation of the pyroxene, aqueous fluids entered into the system and the biotite formed as a result of melt-back reaction. Halogens in these early retrograde fluids could affect the solidus of the footwall granite [64–67] and also affect the transport of base and precious metals in the mineralized section of the Spruce Road area. In order to monitor the activity of the halogens during this early phase of retrograde metamorphism, the halogen content of the biotite II and apatite were investigated.

In the metapelite, the euhedral lath shape of biotite occurring in the leucosome indicates formation of biotite II during the contact metamorphism. A positive correlation between fluorine concentration and Mg# (Figure 6) and the negative correlation between Mg# and chlorine concentration of biotite II indicates that as a result of the "Fe–F and Mg–Cl avoidance rule" [68,69], the chlorine and fluorine content of the biotite are only a function of the temperature. However, in the mineralized

charnockitic samples, the Mg# shows positive correlation with the chlorine content of biotite II. Therefore, the chlorine content of biotite II could have also been controlled by the halogen fugacities of the syn- or early retrograde metamorphic fluids.

The F/Cl and the F/OH ratios of biotite are widely used to determine the variation of $f(H_2O)/f(HF)$ and $f(H_2O)/f(HF)$ ratios of fluids in equilibrium with biotite [49,68,69]. For fugacity ratio calculations, only the euhedral and subhedral rosette-like biotite II were selected. This replaces orthopyroxene and could, therefore, be in equilibrium with the high-temperature metamorphic fluids during the earliest phase of the retrograde metamorphism. Resorbed and corroded prograde biotite I in the core of the orthopyroxene is not included in the calculation because it does not reflect high-temperature equilibrium with early retrograde metamorphic fluids. The $\log(f_{HF}/f_{HCl})_{\text{fluid}}$ and $\log(f_{H2O}/f_{HF})_{\text{fluid}}$ of metamorphic fluids is calculated for the mineralized charnockitic samples, assuming an equilibrium temperature of 850 °C for the proximal samples and 750 °C for the distal samples. For the barren charnockitic samples, no fugacity values are calculated due to the very low Cl content of biotite.

Equations for calculation of fugacity ratios [49–51,68,69] are given below:

$$\log(f_{HF}/f_{HCl})_{\text{fluid}} = 1000/T[1.22 + 1.65(X_{Mg})_{\text{biotite}}] + 0.25 + \log(X_F/X_{Cl})_{\text{biotite}} \quad (5)$$

$$\log(f_{H2O}/f_{HF})_{\text{fluid}} = 1000/T[2.37 + 1.1(X_{Mg})_{\text{biotite}}] + 0.43 - \log(X_F/X_{OH})_{\text{biotite}} \quad (6)$$

where $T$ is temperature (°K) of the halogen exchange, $X_{Mg}$ is the mole fraction of Mg in the octahedral site and $X_{H2O}$, $X_F$, and $X_{Cl}$ are mole fractions of OH, F, and Cl in the hydroxyl site of biotite. Variation of the obtained $\log(f_{HF}/f_{HCl})$ values as a function of distance from the contact is plotted in Figure 10.

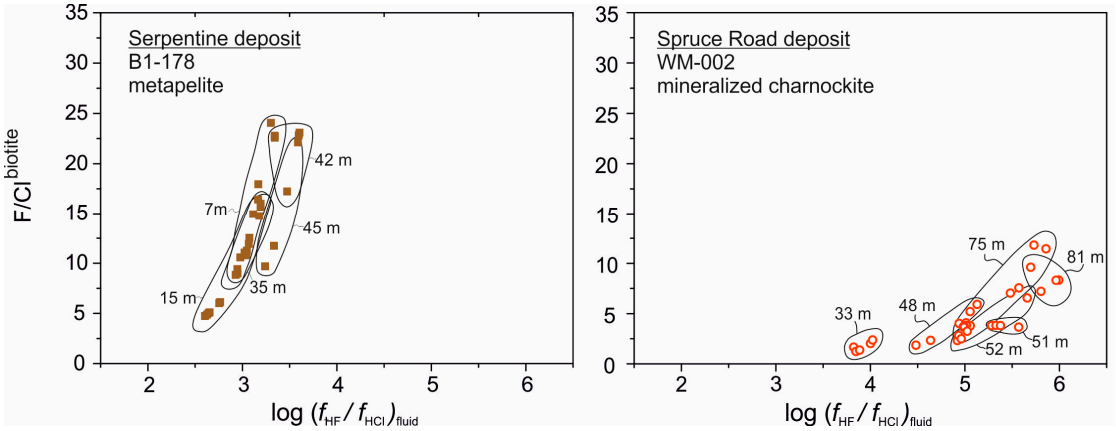



**Figure 10.** F/Cl in biotite (on the basis of apfu) versus $\log(f_{HF}/f_{HCl})_{\text{fluid}}$ diagram for the B1-178 and WM-002 drill cores for the fluids that last equilibrated with the biotite. Note that with increasing depth (distance from the intrusion-footwall contact shown as meter values next to the delineated groups of data points), the $\log(f_{HF}/f_{HCl})_{\text{fluid}}$ is increasing, i.e., the activity of chlorine is decreasing. Positive correlation between $F/Cl^{\text{biotite}}$ and $\log(f_{HF}/f_{HCl})$ proves that independent of the F-Cl avoidance effects, the F/Cl ratio in biotite is simply the function of the F/Cl ratio of the parent metamorphic fluids.

The two halogens (F, Cl) affect the liquidus of a haplogranite system in opposite ways; adding volatiles to the system like F or Li may result in decreasing of the solidus [64,67]. In turn, according to experimental studies in the haplogranite-$H_2O$-NaCl-KCl system, rising chlorine content of the fluid phase present at shallow crustal conditions (0.5–2 kbar) increases the melting temperature [67]. The $\log(f_{HF}/f_{HCl})$ clearly increases with depth in the mineralized charnockite, therefore the increasing activity of the fluorine may have supported melting of the granite, even in the distal zones of the contact aureole (up to 125 m). Evaluation of the $\log(f_{HF}/f_{HCl})$ ratio in the barren charnockite was not

possible as the chlorine concentration in the biotite was under the detection limit. In the unmineralized metapelite, however, no linear correlation was observed between the F/Cl, $\log(f_{HF}/f_{HCl})$, and depth.

Variation of the $\log(f_{H2O}/f_{HF})_{\text{fluid}}$ ratios similar to the F/OH ratios show two different trends. With increasing depth in the mineralized charnockite, the $\log(f_{H2O}/f_{HF})_{\text{fluid}}$ ratios decrease, whereas $\log(f_{H2O}/f_{HF})_{\text{fluid}}$ ratio increases in the barren charnockite (Figure 11). Therefore, in the distal zones of the mineralized drill cores, the fugacity of fluorine in the fluids in equilibrium with biotite II was higher than in the proximal zones. This variation might be due to differences of the fluid migration paths in the footwall.

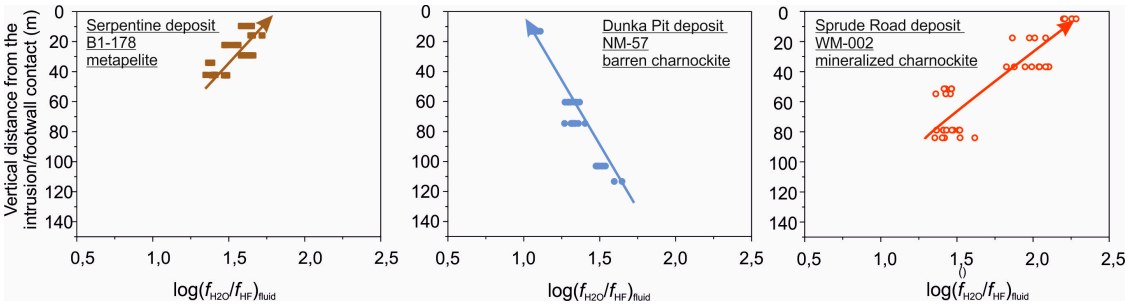



**Figure 11.** Variation of $\log(f_{H2O}/f_{HF})_{\text{fluid}}$ calculated on the basis of biotite halogen ratios as a function of depth in the footwall section of the studied drill cores. The top of the plots coincides with the intrusion-footwall contact. Note that the $\log(f_{H2O}/f_{HF})_{\text{fluid}}$ increases only in the barren NM-57 drill core, i.e., with increasing depth, the fugacity of F decreases. In the mineralized drill cores, the decreasing $\log(f_{H2O}/f_{HF})_{\text{fluid}}$ suggests increasing F fugacity in the distal part of the footwall.

### *5.4. Variation of Halogen Fugacity of the Syn-Metamorphic Fluids in the Footwall on the Basis of Halogen Concentrations in Apatite*

Fluorine and chlorine partitioning between fluid and minerals is mainly influenced by pH, pressure, and fluid halogen compositions [28]. Furthermore, concentration of fluorine and chlorine in apatite is independent of the host mineral chemistry. As pH and pressure can be taken as constant, halogen ratios in apatite that crystallizes during the peak- or during early-retrograde metamorphism will reflect the halogen concentrations of the post/syn-metamorphic fluids. Therefore, apatite is a powerful mineral for monitoring and calculating the halogen fugacity variations and Cl molalities in various magmatic and hydrothermal systems [4,28,49–51,69,70].

In order to use the halogen ratios, the metamorphic origin of apatite has to be proven. In the studied drill cores, apatite is intimately intergrown with rosette-like biotite II. This rosette-like biotite II is formed by crystallization from the partial melt or by retrograde alteration of orthopyroxene. The apatite intergrown with biotite is euhedral, with no corrosion texture on the crystal edges. Therefore, the apatite in the drill cores grew probably during, or subsequent to, the contact metamorphism. A systematic increase in the abundance of chlorine and Cl/F ratio in the apatite with depth in the mineralized charnockite (Figure 6) has been documented, whereas both parameters decrease systematically in the barren charnockite and metapleite.

Under metamorphic conditions, halogen compositions of apatite typically fall along the F-OH join and are characteristically F-rich [71]. This is also true for the apatite in granite far (15 km) from the Duluth Complex (Table 4.). During the crystallization of apatite, Cl and OH are generally excluded from the crystal structure owing to the larger ionic radii of Cl and OH relative to F, and the Cl partition into the fluid phase [71,72]. However, the Cl/F and Cl/OH ratio is also a function of the salinity, temperature, pressure, and activity of the HCl of the syngenetic fluids. The fugacity ratio $f_{HCl}/f_{H2O}$ of the syngenetic fluids coexisting with apatite can be calculated according to [72]:

$$\frac{f_{HCl}^{aq}}{f_{H2O}^{aq}} = \frac{X_{CAp}^{Ap}}{X_{HAp}^{Ap}} \times \frac{1}{10^{\left(0.04661+\frac{2535.8}{T}-\frac{0.0303\times(P-1)}{T}\right)}} \quad (7)$$

where $X_{ClAp}^{Ap}$ and $X_{HAp}^{Ap}$ are the mole fractions of chlor- and hydroxylapatite, $T$ is the temperature of apatite crystallization (Kelvin), and $P$ is the pressure (bars). The temperature in all drill cores was calculated at a fixed pressure of 1700 bars, according to the calculations in a previous study [38]. An average temperature of halogen exchange was considered to be 850 °C in the mineralized charnockite and in the metapelite, and 750 °C in the barren charnockite. Variation in temperature as a function of depth was neglected in this calculation since 100–150 °C variation does not affect the calculations significantly.

The variation of the $f_{HCl}/f_{H2O}$ ratio (Figure 12) in the drill cores prove that: (1) the $f_{HCl}/f_{H2O}$ ratio of the syn-metamorphic fluid was low in all drill cores, and (2) the $f_{HCl}/f_{H2O}$ ratio of the fluids increases with increasing depth in the charnockite but does not vary considerably in the barren charnockite and in the metapelite. This implies that during the peak- or early-retrograde metamorphism, external fluids with higher HCl fugacity mixed with local syn-metamorphic fluids, characterized by lower HCl fugacity at the Spruce Road deposit. The lack of mixing of fluids with contrasting HCl fugacities shows that the unmineralized sites of the footwall at the Dunka Pit and Serpentine deposits were less exposed to the percolation of external fluids. This might be due to the lower peak temperature of the metamorphism at these deposits, or due to local hydrogeological reasons (orientation of fractures or fracture controlled permeability).

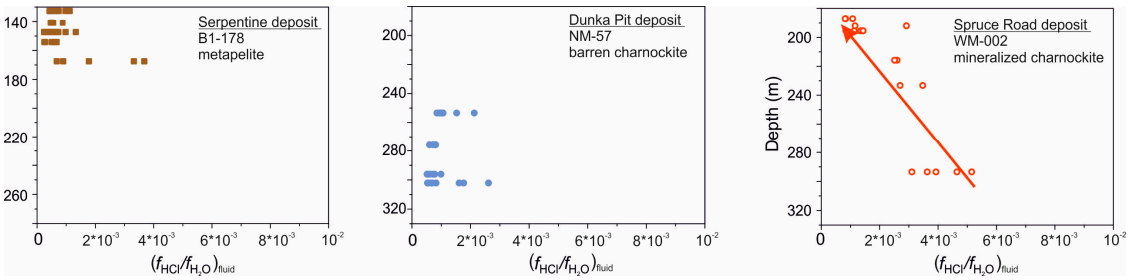



**Figure 12.** Variation of the $(f_{HCl}/f_{H2O})_{\text{fluid}}$ ratios of the fluids in equilibrium with apatite during metamorphism. The top of the plots coincides with the intrusion-footwall contact. Fugacity of chlorine shows a distinct increasing trend with increasing depth in the footwall in the studied mineralized drill cores. In the barren drill core, however, the $(f_{HCl}/f_{H2O})_{\text{fluid}}$ ratio decreases.

Molality of HCl ($m_{HCl}^{aq}$) of the syn-metamorphic fluid can be calculated invoking the Lewis-Randall rule and assuming that the fugacity coefficient ratio is 1:

$$m_{HCl}^{aq} = \frac{X_{CAp}^{Ap}}{X_{HAp}^{Ap}} \times \frac{1000}{18} \times \frac{1}{10^{(0.04661 + \frac{2535.8}{T} - \frac{0.0303 \times (P-1)}{T})}} \quad (8)$$

The molality of the two samples, having the highest $(f_{HCl}/f_{H2O})_{\text{fluid}}$ (0.014 in the mineralized charnockite) and the lowest $(f_{HCl}/f_{H2O})_{\text{fluid}}$ (0.000243 in the metapelite) was calculated. The $(f_{HCl}/f_{H2O})_{\text{fluid}}$ ratio of 0.014 and 0.000243 based on Equation (8) corresponds to a molality of 0.81 and 0.13 ($m_{HCl}^{aq}$), respectively. Assuming that the cations in the syn-metamorphic fluids were all monovalent Na ions, the salinity of the fluids expressed in NaCl as equivalent weight % can be calculated. The molality of 0.81 recalculated to weight percent is 0.84 NaCl equivalent weight % and the molality of 0.13 corresponds to 0.14 NaCl equivalent weight %.

### *5.5. Implication of the Variation of Halogens in the Early-Retrograde Fluids on the Cu-Ni-PGE Mineralization in the Charnockitic Footwall*

Apatite formed under metamorphic and magmatic conditions are characteristically fluorine-rich [61]. Accordingly, apatite in the uncontaminated footwall granite is F-rich, with chlorine concentrations near to the detection limit of the SEM-EDX. Therefore, the metamorphic fluids in the

mineralized charnockite at the Spruce Road deposit could not be solely responsible for the observed halogen concentration ratios, and variations in the apatite and another fluid must be involved.

Variation of halogen concentrations and salinities of fluids in the footwall of other mafic intrusions were also reported [3,5,73–84]. The candidates for the source of fluids in these studies are: (1) magmatic fluids that exsolved from the mafic intrusion, (2) magmatic fluids that exsolved from the sulfide liquid, (3) regional groundwater-metamorphic fluids, or (4) fluids released during partial melting. Magmatic fluids exsolving from the sulfide liquid do not explain the halogen variations in the barren charnockite and are unlikely voluminous enough to result in variations in the studied extent [79,80]. However, the strong textural relationship between the chalcopyrite + bornite + PGM assemblage and biotite (Figure 3d) suggest that some fluids may have had exsolved from the sulfide liquid. Alternatively, the sulfide-biotite association might simply reflect the effectiveness of sulfide liquid infiltration, where partial melt porosity was more developed in the footwall rocks. Magmatic fluids exsolving from the mafic magma often transport voluminous base and precious metals and are responsible for chromatographic separation of these metals [81–86]. As a result of the segregation of the chlorine-rich fluid, the apatite at the place of segregation is fluorine-rich. The degassed chlorine-rich fluid can transport significant amounts of sulfur and PGE, at least on a local scale. Once the degassed fluid encounters physical–chemical discontinuity (change in fluid saturation, temperature) the S, base metals, and PGE will precipitate [80]. However, major drawbacks of the application of this model in the footwall are that: (1) fluids migrate primarily upwards in the studied mafic-ultramafic systems (Bushveld and Stillwater Complexes), (2) mineralization in the referred intrusions are reef-type, whereas the texture of the sulfide ore is disseminated and no distinct reef-type or stratiform ore was observed in the footwall. Fluids released during the dehydration of the footwall granite are also unlikely to assist to the mineralization because: (1) they were probably not voluminous enough, and (2) the opposite trends of halogen ratio variations (increase of Cl/F ratios with depth) are not conformable with this model (upward increase of the Cl/F ratios).

Finally, the fourth source of the fluids could be the dehydration of $H_2O$ and OH bearing minerals (biotite and amphiboles) during the contact metamorphism. Mineral reactions (e.g., Equation (3)) result in the liberation of $H_2O$ from hydrous minerals. Furthermore, strong temperature variations and mineral zonation in the contact aureole can led to variation of Cl/F ratios and their activities.

Local convection cells might be also responsible for the contrasting halogen-ratio variations in the barren vs. mineralized charnockite. Fluor-rich apatite far from the contact is likely of granitic origin that was not in contact with high salinity formational fluids. Apatite Cl/F ratios at the Dunka Pit and Serpentine deposits either reflect the magmatic and metapelitic very low Cl/F ratios, or only low salinity fluids at this segment of the contact aureole, derived from the intrusion, were present during the contact metamorphism. The most probable candidate responsible for the high Cl/F concentration of apatite and biotite is saline groundwater, which is characteristic of the Archean shield [85]. These fluids may have continuously percolated into the contact aureole and mixed with low salinity local fluids [86] that may have exsolved from the intrusion or liberated during the contact metamorphism.

There are only limited experimental results on the high temperature mobility and complexing of PGEs. Experimental studies [87,88], observations on natural systems in the Bushveld Complex [89], and the Sudbury Igneous Complex [5,90] showed that at the high temperature magmatic-hydrothermal transition, high-salinity volatiles can potentially transport economically significant amounts of Pt, Pd, and Au at moderately oxidizing conditions. Transport at these temperatures (600–1000 °C) is controlled primarily by HCl or hydroxide complexes, but with decreasing temperature, the significance of bisulfide complexes is increasing [38,91–93].

Halogen concentrations in the syn- and early retrograde metamorphic fluids could have been twofold: (1) indirectly, the variation of the Cl/F ratio may have controlled the solidus of the rock and this may have extended the thickness of the permeable zone in which the sulfide liquid penetrated Zsolt and/or (2) metamorphic fluids played a direct role in base and precious metal transport.

As was demonstrated above, the variation of halogen fugacity clearly promoted partial melting in the mineralized charnockite. However, the evaluation of the role of metamorphic fluids in direct base-metals, precious metals, and sulfur transport is more difficult.

The calculated salinities of the syn-metamorphic fluids 0.14–0.84 NaCl equivalent weight % are, however, significantly lower than those observed in the footwall of the Sudbury complex and in the Bushveld or Stillwater complexes [5,89,90]. Therefore, the early, syn-metamorphic aqueous fluids probably did not play a significant role in precious metal transport but may have contributed only to the base metal mobilization. The observed covariance of halogen fugacity and Pd/Rh ratios [22] in the mineralized drill core (Figure 13) cannot be accounted to the fluid transport of precious metals directly, but to the variations of halogens in the metamorphic fluids that supported melting of the rock and indirectly permitted the sulfide liquid to penetrate and fractionate downwards [22].

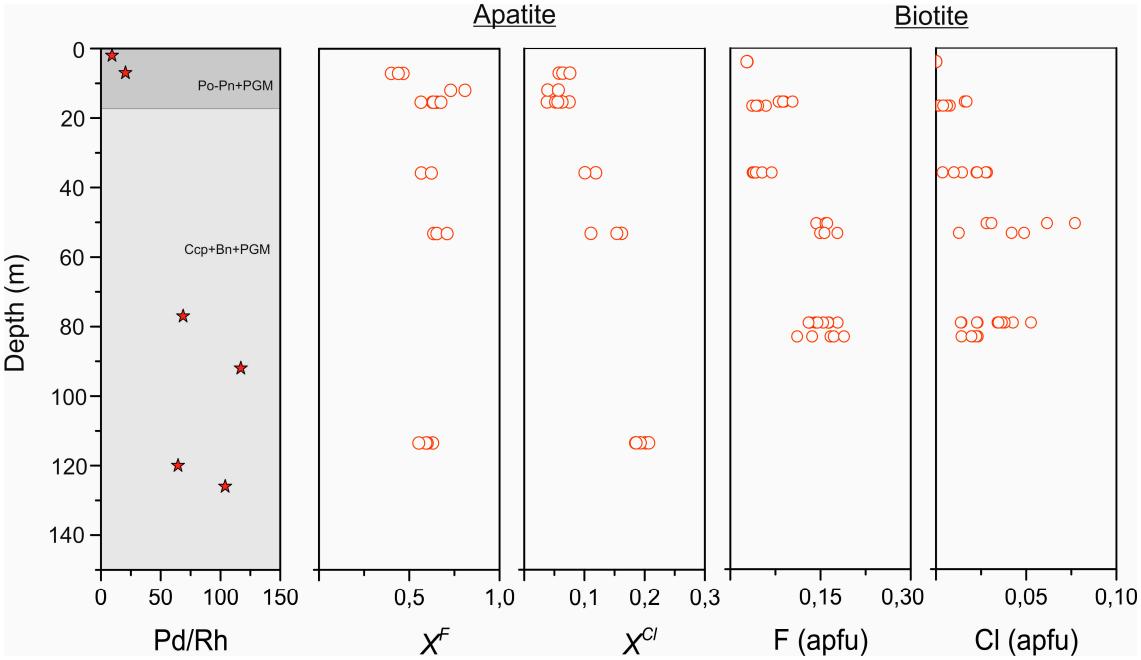



**Figure 13.** A simplified plot of variation of $X^{Cl}$ and $X^F$ in apatite and atomic proportions per formula unit of Cl and F in biotite versus Pd/Rh ratios in the mineralized drill core. Pd/Rh data are from a previous study [22]. The top of the plots coincides with the intrusion-footwall contact. (Po = pyrrhotite, Pn = Pentlandite, Ccp = Chalopyrite, Bn = Bornite, PGM = Platinum Group Minerals).

## 6. Conclusions

We investigated whether thermal profiles along the contact zones under the South Kawishiwi intrusion influence the absence or presence of PGE enriched footwall ores. Based on the above considerations, the following conclusions can be drawn: except for the mineralized drill core (WM-002; Spruce Road deposit), all mineral thermometers, including the two-pyroxene, biotite-apatite, and the titanium-in-quartz thermometers, provided consistent and comparable data. These data are consistent with the temperatures derived previously from mineral reactions and fluid inclusion data. The good fit of the data proves that these thermometers are applicable in contact metamorphic aureoles of large mafic intrusions.

In the mineralized segment of the South Kawishiwi intrusion, high temperature (820–950 °C) can be affirmed during the contact metamorphism, whereas in the unmineralized zone of the footwall, the maximum temperature was lower (~800 °C). The new observation confirms that footwall mineralization is confined in some thermally anomalous zones of metamorphosed granitic footwall. The zones are most likely the zones of magma conduits channeling persistent or pulsing magma flow. Sulfide liquid could penetrate from the bottom of these channels into the partially molten charnockite.

Variation of chlorine and fluorine activity in the syn-metamorpohic fluids further enhanced differences in the degree of partial melting. The increasing fluorine concentration in the mineralized drill core could have slightly decreased the solidus of the rock and therefore indirectly supported the infiltration of the sulfide liquid into the partially molten charnockite.

Enrichment of Cu, Pd, and Pt in the mineralized segment of the contact aureole are consistent with the sulfide liquid fractional crystallization that was suggested previously [22]. Therefore, evolved sulfide liquids could infiltrate the molten footwall rock through the porosity, and sulfides evolve as temperature decreases away from the contact.

**Author Contributions:** Z.B. analyzed the samples conceived the results and wrote the paper. A.M. and F.M. established the financial background, prepared, supervised and organized the research. K.E. supported the analytical work in Graz, Austria. S.A.H. and M.J.S. organized and supported the visit at the NRRI and in the drill core library, Hibbing, Minnesota, USA. They gave access to the NRRI drill core data base and research reports.

**Funding:** We acknowledge the financial support of the Austrian Science Fund (FWF–P23157–N21) to Aberra Mogessie and the Senior Fellowship support to Ferenc Molnar by the Hungarian–American Enterprise Scholarship Fund and internal funding from the Natural Resources Research Institute, University of Minnesota Duluth. The research was also supported by the European Union and the State of Hungary, co-financed by the European Regional Development Fund in the project of GINOP-2.3.2.-15-2016-00009 'ICER'.

**Acknowledgments:** The manuscript has been significantly improved by thorough comments from Craig Manning, Peter Tropper, and Alan Boudreau. We thank the anonymous reviewers for their careful reading of our manuscript and their many insightful comments and suggestions. A sincere thank you to Timothy Jull for his diligent proofreading of this paper.

**Conflicts of Interest:** The authors declare no conflict of interest.

## References

1. Molnár, F. Pd-Pt-Au rich sulphide ores in footwalls of layered mafic-ultramafic igneous complexes. *Proc. Natl. Acad. Sci. USA* **2013**, *198*, 121–125.
2. Iljina, M.J.; Lee, C.A. PGE Deposits in the Marginal Series of Layered Intrusions. In *Exploration in Platinum-Group Elements Deposit*; Mungall, J., Ed.; Mineralogical Association of Canada Short Course Series Volume; Mineralogical Association of Canada: Quebec City, QC, Canada, 2005; Volume 35, pp. 75–96.
3. Péntek, A.; Molnár, F.; Watkinson, D.H.; Jones, P.C.; Mogessie, A. Partial melting and melt segregation in footwall units within the contact aureole of the Sudbury Igneous Complex (North and East Ranges, Sudbury structure), with implications for their relationship to footwall Cu-Ni-PGE mineralization. *Int. Geol. Rev.* **2011**, *53*, 291–325. [CrossRef]
4. Péntek, A.; Molnár, F.; Tuba, G.; Watkinson, D.H.; Jones, P.C. The significance of partial melting processes in hydrothermal low sulfide Cu–Ni–PGE mineralization within the footwall of the Sudbury Igneous Complex, Ontario, Canada. *Econ. Geol.* **2013**, *108*, 59–78. [CrossRef]
5. Molnár, F.; Watkinson, D.H.; Jones, P.C. Multiple hydrothermal processes in footwall units of the North Range, Sudbury Igneous Complex, Canada, and implications for the genesis of vein–type Cu–Ni–PGE deposits. *Econ. Geol.* **2001**, *96*, 1645–1670. [CrossRef]
6. Tuba, G.; Molnár, F.; Watkinson, D.H.; Jones, P.C. Characterization of hydrothermal vein and alteration assemblages associated with 'low–sulfide' footwall Cu–Ni–PGE mineralization and regional hydrothermal processes, North and East Ranges, Sudbury structure, Canada. *Soc. Econ. Geol. Spéc. Publ.* **2010**, *15*, 573–598.
7. Tuba, G.; Molnár, F.; Ames, D.A.; Péntek, A.; Watkinson, D.H.; Jones, P.C. Multi–stage hydrothermal processes involved in 'low–sulfide' Cu(–Ni)–PGE mineralization in the footwall of the Sudbury Igneous Complex (Canada): Amy Lake PGE zone, East Range. *Miner. Deposita* **2013**, *49*, 7–47. [CrossRef]
8. Thériault, R.D.; Barnes, S.-J.; Severson, M.J. Origin of Cu–Ni–PGE mineralization in the Partridge River Intrusion, Duluth Complex, Minnesota. *Econ. Geol.* **2000**, *95*, 929–943.
9. Barnes, J.S.; Cruden, R.A.; Arndt, N.; Saumur, M.B. The mineral system approach applied to Ni—Cu—PGE sulphide deposits. *Ore Geol. Rev.* **2015**, *76*, 296–316. [CrossRef]
10. Saumur, B.M.; Cruden, A.R. Ingress of magmatic Ni-Cu sulphide liquid into surrounding brittle rocks: Physical & structural controls. *Ore Geol. Rev.* **2017**, *90*, 439–445.

11. Holwell, D.A.; McDonald, I.; Armitage, P.E.B. Platinum-group mineral assemblages in the Platreef at the Sandsloot Mine, northern Bushveld Complex, South Africa. *Miner. Mag.* **2006**, *70*, 83–101. [CrossRef]
12. Patelke, R. *Exploration Drill Hole Lithology, Geologic Unit, Copper–Nickel Assay, and Location Database for the Keweenawan Duluth Complex, Northeastern Minnesota*; Technical Report NRRI/TR–2003/21; University of Minnesota Duluth, Natural Resources Research Institute: Duluth, MN, USA, 2003; 97p.
13. Peterson, D.M. *Ore Deposit Modeling and Mineral Exploration Criteria for Footwall Copper-Nickel-Platinum Group Element Mineralization in the Duluth Complex*; Report; Minnesota Department of Natural Resources, Division of Minerals: Carson City, NV, USA, 1997; Volume 317, pp. 1–40.
14. Samalens, N.; Barnes, S.-J.; Sawyer, E.W. The role of black shales as a source of sulfur and semimetals in magmatic nickel-copper deposits: Example from the Partridge River Intrusion, Duluth Complex, Minnesota, USA. *Ore Geol. Rev.* **2017**, *81*, 173–187. [CrossRef]
15. Peterson, D.M. Nokomis Deposit—Duluth Metals. In *Cu–Ni–PGE Deposits in Mafic Intrusions of the Lake Superior Region, Guidebook for Post–Symposium Field Trip B2, Proceedings of the 11th International Platinum Symposium, Sudbury, ON, Canada, 21–24 June 2010*; Miller, J.D., Smyk, M.C., Hollings, P.N., Eds.; Ontario Geological Survey: Sudbury, ON, Canada; pp. 97–116.
16. Sawyer, E.W. *Report on Thin Sections from DDH WM–1, Spruce Road Cu–Ni Deposit, South Kawishiwi Intrusion, Duluth Complex*; Report of Investigations, NRRI/RI–2002/13; University of Minnesota Duluth, Natural Resources Research Institute: Duluth, MN, USA, 2002; 21p.
17. Sawyer, E.W. The inception and growth of leucosomes: Microstructure at the start of melt segregation in migmatites. *J. Metamorph. Petrol.* **2014**, *32*, 695–712. [CrossRef]
18. Benkó, Z.; Molnár, F.; Mogessie, A.; Severson, M.; Hauck, S.A.; Arehart, G.A. Cu-Ni-Au-PGE transport in the partially molten charnockitic footwall of the Spruce Road deposit, South Kawishiwi Intrusion, Duluth Complex, Minnesota, USA. Mineral Deposit Research for a High-Tech World. In Proceedings of the 12th SGA Biennial Meeting, Uppsala, Sweden, 12–15 August 2013; pp. 952–955.
19. Benkó, Z.; Molnár, F.; Mogessie, A.; Severson, M.J.; Hauck, S.A.; Arehart, G.A. Cu-Ni-PGE mineralization of felsic dikes along the Grano fault in the Bathtub Intrusion (Duluth Complex, Minnesota, USA). Mineral deposit research for a high-tech world. In Proceedings of the 12th SGA Biennial Meeting, Uppsala, Sweden, 12–15 August 2013; pp. 948–951.
20. Peterson, D.M. *Shaded Relief Map of the Basal Contact Surface of the South Kawishiwi Intrusion Duluth Complex, Northeastern Minnesota*; NRRI/MAP-2002/02; Natural Resources Research Institute: Duluth, MN, USA, 2002.
21. Hovis, S.T. *Observations on Cu-Ni Mineralization in the Giants Range Batholith Footwall to the South Kawishiwi Intrusion, Duluth Complex, Northeastern Minnesota*; Report of Investigations NRRI/TR-2003/24; University of Minnesota Duluth, Natural Resources Research Institute: Duluth, MN, USA, 2003; p. 36.
22. Benkó, Z.; Mogessie, A.; Molnár, F.; Severson, M.; Hauck, S.A.; Raic, G.A. Partial melting processes and Cu-Ni-PGE Mineralization in the footwall of the South Kawishiwi intrusion at the Spruce Road Deposit, Duluth Complex, Minnesota. *Econ. Geol.* **2015**, *110*, 1269–1293. [CrossRef]
23. Ballhaus, C.G.; Stumpfl, E.F. Sulfide and platinum mineralization in the Merensky Reef: Evidence from hydrous silicates and fluid inclusions. *Contrib. Miner. Petrol.* **1986**, *94*, 193–204. [CrossRef]
24. Hanley, J.J. The aqueous geochemistry of the Platinum Group Elements (PGE) in surficial, low-T hydrothermal and high-T magmatic-hydrothermal environments. In *Exploration for Platinum Group Element Deposits*; Mungall, J., Ed.; Short Course Series Volume; Mineralogical Association of Canada: Oulu, Finland, 6–7 August 2005; Volume 35, pp. 35–56.
25. Naney, M.T. Phase equilibria of rock forming ferromagnesian silicates in granitic systems. *Am. J. Sci.* **1983**, *283*, 993–1033. [CrossRef]
26. Lindsley, D.H. Pyroxene thermometry. *Am. Miner.* **1983**, *68*, 477–493.
27. Wark, D.A.; Watson, E.B. TitaniQ: A titanium-in-quartz geothermometer. *Contrib. Miner. Petrol.* **2006**, *152*, 743–754. [CrossRef]
28. Zhu, C.; Sverjensky, D.A. F-Cl-OH partitioning between biotite and apatite. *Geochim. Cosmochim. Acta* **1992**, *55*, 3435–3467. [CrossRef]
29. Van Schmus, W.R.; Hinze, W.J. The Midcontinent Rift System. *Annu. Rev. Earth Planet. Sci.* **1985**, *13*, 345–383. [CrossRef]
30. Miller, J.D.; Severson, M.J. Geology of the Duluth Complex. In *Geology and Mineral Potential of the Duluth Complex and Related Rocks of Northeastern Minnesota*; Miller, J.D., Green, J.C., Jr., Severson, M.J., Chandler, V.W.,

Hauck, S.A., Peterson, D.M., Wahl, T.E., Eds.; Report of Investigations; Minnesota Geological Survey: Saint Paul, MN, USA, 2002.
31. Severson, M.J.; Hauck, S.A. *Finish Logging of Duluth Complex Drill Core (and a Reinterpretation of the Geology at the Mesaba (Babbitt) Deposit)*; Technical Report NRRI/TR–2008/17; University of Minnesota Duluth, Natural Resources Research Institute: Duluth, MN, USA, 2008; 68p.
32. Ojakangas, R.W.; Morey, G.B.; Green, J.C. The Mesoproterozoic Midcontinent Rift System, Lake Superior Region, USA. *Sediment. Geol.* **2001**, *141–142*, 421–442. [CrossRef]
33. Naldrett, A.J. *Magmatic sulfide depoits*; Springer Verlag Berlin: Heidelberg, Germany, 2010; pp. 1–17.
34. Severson, M.J. *Igneous Stratigraphy of the South Kawishiwi Intrusion, Duluth Complex, Northwestern Minnesota*; Report of Investigations, NRRI/TR-93/34; University of Minnesota Duluth, Natural Resources Research Institute: Duluth, MN, USA, 1994; p. 210.
35. Gál, B.; Molnár, F.; Peterson, M.D. Cu-Ni-PGE mineralization in the South Filson Creek Area, South Kawishiwi intrusion, Duluth Complex: Mineralization styles, magmatic and hydrothermal processes. *Econ. Geol.* **2011**, *106*, 481–509. [CrossRef]
36. Green, J.C. Lower Precambrian rocks of the Gabbro Lake Quadrangle, Northeastern Minnesota. *Minn. Geol. Surv. Spéc. Publ. Ser.* **1970**, *13*, 96.
37. Sims, P.K.; Viswanathan, S. *Giants Range batholiths In Geology of Minnesota. A Centennial Volume*; Sims, P.K., Morey, G.B., Eds.; Minnesota Geological Survey: Saint Paul, MN, USA, 1972; pp. 120–139.
38. Gál, B.; Molnár, F.; Guzmics, T.; Mogessie, A.; Szabó, C.; Peterson, D.M. Segregation of magmatic fluids and their potential in the mobilization of platinum–group elements in the South Kawishiwi intrusion, Duluth Complex, Minnesota—Evidence from petrography, apatite geochemistry and coexisting fluid and melt inclusions. *Ore Geol. Rev.* **2013**, *54*, 59–80. [CrossRef]
39. Benkó, Z.; Mogessie, A.; Molnár, F.; Krenn, K.; Poulson, S.R.; Hauck, S.A.; Severson, M.; Arehart, G.A. Hydrothermal alteration and Cu–Ni–PGE mobilization in the charnockitic rocks of the footwall of the South Kawishiwi intrusion, Duluth Complex, USA. *Ore Geol. Rev.* **2015**, *67*, 170–188. [CrossRef] [PubMed]
40. Lucente, M.E.; Morey, G.B. Stratigraphy and sedimentology of the Lower Proterozoic Virginia Formation, northern Minnesota. *Minn. Geol. Surv. Rep. Investig.* **1983**, *28*, 28.
41. Zanko, L.M.; Severson, M.J.; Ripley, E.M. *Geology and Mineralization of the Serpentine Copper-Nickel Deposit*; Report of Investigations, NRRI/TR-93/52; University of Minnesota Duluth, Natural Resources Research Institute: Duluth, MN, USA, 1994.
42. Arcuri, T.; Ripley, E.M.; Hauck, S.A. Sulfur and oxygen isotope studies of the interaction between peelitic xenoliths and basaltic magma at the Babbitt and Serpentine Cu-Ni deposits, Duluth Complex, Minnesota. *Econ. Geol.* **1998**, *93*, 1063–1075. [CrossRef]
43. Ripley, E.; Li, C. Sulfide saturation in mafic magmas: Is external sulfur required for magmatic Ni-Cu-(PGE) ore genesis? *Econ. Geol.* **2013**, *108*, 45–58. [CrossRef]
44. Mogessie, A.; Stumpfl, E.F. Platinum-group element and stable isotope geochemistry of PGM-bearing troctolitic rocks of the Duluth Complex, Minnesota. *Aust. J. Earth Sci.* **1992**, *39*, 315–325. [CrossRef]
45. Sawyer, E.W. *Atlas of Migmatites*; National Research Council of Canada: Ottawa, ON, Canada, 2008.
46. Bohlen, S.R.; Essene, E.J. A critical evaluation of two–pyroxene thermometry in Adirondack granulites. *Lithos* **1979**, *12*, 335–345. [CrossRef]
47. Glassley, W.E.; Sorensen, K. Constant Ps–T amphibolite to granulite facies transition in Agto (West Greenland) metadolerites: Implications and applications. *J. Petrol.* **1980**, *21*, 69–105. [CrossRef]
48. Pitra, P.; De Waal, S.A. High-temperature, low-pressure metamorphism and development of prograde symplectites, Marble Hall Fragment, Bushveld Complex (South Africa). *J. Metamorph. Petrol.* **2008**, *19*, 311–325. [CrossRef]
49. Zhu, C.; Sverjensky, D.A. Partitioning of F-Cl-OH between minerals and hydrothermal fluids. *Geochim. Cosmochim. Acta* **1991**, *55*, 1837–1858. [CrossRef]
50. Sallet, R. Fluorine as a tool in the petrogenesis of quartz-bearing magmatic associations: Applications of an improved F-OH biotite-apatite thermometer grid. *Lithos* **2000**, *50*, 241–253. [CrossRef]

51. Bath, A.B.; Walshe, J.L.; Cloutier, J.; Verrall, M.; Cleverley, J.S.; Pownceby, M.I.; Macrae, C.M.; Wilson, C.N.; Tunjic, J.; Nortje, G.S.; et al. Biotite and apatite as tools for tracking pathways of oxidized fluids in the Archean East Repulse gold deposit, Australia. *Econ. Geol.* **2013**, *108*, 667–690. [CrossRef]
52. Petcovic, H.L.; Grunder, A.L. Textural and thermal history of partial melting in tonalitic wallrock at the margin of a basalt dike, Wallowa Mountains, Oregon. *J. Petrol.* **2003**, *44*, 2287–2313. [CrossRef]
53. Vielzeuf, D.; Montel, J.M. Partial melting of metagreywackes. Part I: Fluid absent experiments and phase relationships. *Contrib. Miner. Petrol.* **1994**, *98*, 257–276.
54. Montel, J.M.; Vielzeuf, D. Partial melting of metagreywackes Part II. Compositions of minerals and melts. *Contrib. Miner. Petrol.* **1997**, *128*, 176–196. [CrossRef]
55. Patiño Douce, A.E.; Beard, J.S. Dehydration-meting of biotite gneiss and amphibolite from 36 kbar to 16 kbar. *J. Petrol.* **1995**, *36*, 707–738. [CrossRef]
56. Naldrett, A.J. *Magmatic Sulfide Deposits*; Springer-Verlag Berlin: Heidelberg, Germany, 2010; pp. 1–727.
57. Duran, C.J.; Barnes, S.J.; Pleše, P.; Kudrna Prašek, M.; Zientek, M.L.; Pagé, P. Fractional crystallization-induced variations in sulfides from the Norilsk-Talnakh mining district (polar Siberia, Russia). *Ore Geol. Rev.* **2017**, *90*, 326–351. [CrossRef]
58. Dare, S.A.S.; Barnes, S.-J.; Prichard, H.M.; Fisher, P.C. Mineralogy and Geochemistry of Cu-Rich Ores from the McCreedy East Ni-Cu-PGE Deposit (Sudbury, Canada): Implications for the Behavior of Platinum Group and Chalcophile Elements at the End of Crystallization of a Sulfide Liquid. *Econ. Geol.* **2014**, *109*, 343–366. [CrossRef]
59. Liu, Y.; Brenan, J. Partitioning of platinum-group elements (PGE) and chalcogens (Se, Te, As, Sb, Bi) between monosulfide-solid solution (MSS), intermediate solid solution (ISS) and sulfide liquid at controlled fO2-fS2 conditions. *Geochim. Cosmochim. Acta* **2015**, *159*, 139–161. [CrossRef]
60. Kullerud, G.; Yund, R.A.; Moh, G.H. Phase relations in the Cu–Fe–S, Cu–Ni–S, and Fe–Ni–S systems. In *Magmatic Ore Deposits*; Wilson, H.D.B., Ed.; Economic Geology Monograph 4; Society of Economic Geologists: Littleton, CO, USA, 1969; pp. 1–366.
61. Ebel, D.S.; Naldrett, A.J. Fractional crystallization of sulfide ore liquids at high temperature. *Econ. Geol.* **1996**, *91*, 607–621. [CrossRef]
62. Tsujimura, T.; Kitakaze, A. New phase relations in the Cu-Fe-S system at 800 °C; constraint of fractional crystallization of a sulfide liquid. *Neues Jahrb. Mineral. Monatshefte* **2004**, *10*, 433–444. [CrossRef]
63. Zhao, J.; Brugger, J.; Ngothai, Y.; Pring, A. The replacement of chalcopyrite by bornite under hydrothermal conditions. *Am. Miner.* **2014**, *99*, 2389–2397. [CrossRef]
64. Manning, D.A.C. The effect of fluorine on liquidus phase relationships in the system Qz–Ab–Or with excess water at 1 kbar. *Contrib. Miner. Petrol.* **1981**, *76*, 206–215. [CrossRef]
65. Xiong, X.-L.; Zhao, Z.-H.; Zhu, J.-C.; Bing, R. Phase relations in albite granite–$H_2O$–HF system and their petrogenetic applications. *Geochem. J.* **1999**, *33*, 199–214.
66. Aranovich, L.Y.; Newton, R.C.; Manning, C.E. Brine-assisted anatexis: Experimental melting in the system haplogranite-$H_2O$-NaCl-KCl at deep-crustal conditions. *Earth. Plan. Sci. Lett.* **2013**, *374*, 111–120. [CrossRef]
67. Manning, C.E.; Aranovich, L.Y. Brines at high pressure and temperature: Thermodynamic, petrologic and geochemical effects. *Precambr. Res.* **2014**, *253*, 6–16. [CrossRef]
68. Munoz, J.L. Calculation of HF and HCl fugacities from biotite compositions: Revised equations. *Geol. Soc. Am. Abstr. Progr.* **1992**, *24*, A221.
69. Munoz, J.L. F–OH and Cl–OH exchange in micas with applications to hydrothermal ore deposits. In *Micas*; Bailey, S.W., Ed.; Reviews in Mineralogy; Mineralogical Society of America: Washington, DC, USA, 1987; Volume 13, pp. 469–493.
70. Korzhinsky, M.A. Apatite solid solutions as indicators of the fugacity of HCl and HF in hydrothermal fluids. *Geochem. Int.* **1981**, *3*, 45–60.
71. Spear, F.S.; Pyle, J.M. Apatite, monazite and xenotime in metamorphic rocks. In *Phosphates: Geochemical, Geobiological, and Materials Importance*; Kohn, M.J., Rakovan, J., Hughes, J.M., Eds.; Reviews in Mineralogy and Geochemistry 48; Mineralogical Society of America: Washington, DC, USA, 2002; pp. 293–336.

72. Piccoli, P.M.; Candela, P.A. Apatite in felsic rocks: A model for the estimation of initial halogen contents in the Bishop Tuff (Long Valley) and Tuolumne Intrusive Suite (Sierra Nevada Batholith) Magmas. *Am. J. Sci.* **1994**, *294*, 92–135. [CrossRef]
73. Li, C.; Naldrett, A.J.; Coats, C.J.A.; Johannessen, P. Platinum, palladium, gold and copper-rich stringers at the Strathcona mine, Sudbury: Their enrichment by fractionation of a sulfide liquid. *Econ. Geol.* **1992**, *87*, 1584–1598. [CrossRef]
74. Jago, B.C.; Morrison, G.G.; Little, T.L. Metal zonation patterns and microtextural and micromineralogical evidence for alkali- and halogen rich fluids in the genesis of the Victor Deep and McCreedy East footwall copper orebodies, Sudbury Igneous Complex. *Ont. Geol. Surv. Spéc. Vol.* **1994**, *5*, 65–75.
75. Marshall, D.D.; Watkinson, D.H.; Farrow, C.E.G.; Molnár, F.; Fouillac, A.M. Multiple fluid generations in the Sudbury Igneous Complex: Fluid inclusion, Ar, O, Rb and Sr evidence. *Chem. Geol.* **1999**, *157*, 1–19. [CrossRef]
76. Hanley, J.J.; Mungall, J.E. Chlorine enrichment and hydrous alteration of the Sudbury breccia hosting footwall Cu-Ni-PGE mineralization at the Fraser mine, Sudbury, Ontario, Canada. *Can. Miner.* **2003**, *41*, 857–881. [CrossRef]
77. Mungall, J.E.; Brenan, J.M. Experimantal evidence for the chalcophile behaviour of the halogens. *Can. Miner.* **2003**, *41*, 207–220. [CrossRef]
78. Wykes, J.; Mavrogenes, J. Hydrous sulfide melting: Experimental evidence for the solubility of $H_2O$ in sulfide melts. *Econ. Geol.* **2005**, *100*, 157–164. [CrossRef]
79. Boudreau, A.E.; McCallum, I.S. Infiltration metasomatism in layered intrusions—An example from the Stillwater Complex, Montana. *J. Volcanol. Geoth. Res.* **1992**, *52*, 171–183. [CrossRef]
80. Boudreau, A.E.; Love, C.; Hoatson, D. Halogen geochemistry of the Munni Munni Complex and associated intrusions of the Pilbara Block, W. *Australia. Geochim. Cosmochim. Acta* **2000**, *57*, 4467–4477. [CrossRef]
81. Boudreau, A.E.; Kruger, F.J. Variation in the composition of apatite through the Merensky cyclic unit in the western Bushveld Complex. *Econ. Geol.* **1990**, *85*, 737–745. [CrossRef]
82. Boudreau, A.E. Some geochemical considerations for platinum-group element exploration in layered intrusions. *Explor. Min. Geol.* **1995**, *3*, 215–225.
83. Boudreau, A.E.; Love, C.; Prendergast, M.D. Halogen geochemistry of the Great Dyke, Zimbabwe. *Contrib. Miner. Petrol.* **1995**, *122*, 289–300. [CrossRef]
84. Meurer, W.P.; Boudreau, A.E. Evaluation of models for halogen variations in apatite from layered intrusions using a detailed study of apatite from OB-III and OB-IV of the Middle Banded series, Stillwater Complex, Montana. *Contrib. Miner. Petrol.* **1996**, *123*, 225–236. [CrossRef]
85. Holland, G.; Sherwood-Lollar, B.; Li, L.; Lacrampe-Couloume, G.; Slater, G.F.; Ballentine, C.J. Deep fracture fluids isolated in the crust since the Precambrian era. *Nature* **2013**, *497*, 357–362. [CrossRef] [PubMed]
86. Audétat, A.; Pettke, T.; Heinrich, C.A.; Bodnar, R.J. The composition of magmatic–hydrothermal fluids in barren and mineralized intrusion. *Econ. Geol.* **2008**, *103*, 877–908. [CrossRef]
87. Wood, S.A. The aqueous geochemistry of the platinum-group elements with applications to ore deposits. In *The Geology, Geochemistry, Mineralogy and Mineral Beneficiation of Platinum-Group Elements: Canadian Institute of Mining, Metallurgy and Petroleum*; Cabri, L.J., Ed.; Canadian Institute of Mining, Metallurgy and Petroleum: Montreal, QC, Canada, 2002; Volume 54, pp. 483–506.
88. Hanley, J.J.; Pettke, T.; Mungall, J.E.; Spooner, E.T.C. The solubility of platinum and gold in NaCl brines at 1.5 kbar, 600 to 800 °C: A laser ablation ICP-MS pilot study of synthetic fluid inclusions. *Geochim. Cosmochim. Acta* **2005**, *69*, 2593–2611. [CrossRef]
89. Ballhaus, C.G.; Ryan, C.G.; Mernagh, T.P.; Green, D.H. The partitioning of Fe, Ni, Cu, Pt, and Au between sulphide, metal, and fluid phases: A pilot study. *Geochim. Cosmochim. Acta* **1994**, *58*, 811–826. [CrossRef]
90. Molnár, F.; Watkinson, D.H.; Jones, C.; Gatter, I. Fluid inclusion evidence for hydrothermal enrichment of magmatic ore at the contact zone of the 4b Ni-Cu-PGE deposit, Lindsley Mine, Sudbury, Canada. *Econ. Geol.* **1997**, *92*, 674–685. [CrossRef]
91. Gammons, C.H.; Bloom, M.S. Experimental investigation of the hydrothermal geochemistry of platinum and palladium: II. *The solubility of PtS and PdS in aqueous sulfide solutions. Geochim. Cosmochim. Acta* **1993**, *57*, 2451–2467. [CrossRef]

92. Polovina, J.S.; Hudson, M.D.; Jones, R.E. Petrographic and geochemical characteristics of postmagmatic hydrothermal alteration and mineralization in the JM Reef, Stillwater Complex, Montana. *Can. Mineral.* **2004**, *42*, 261–277. [CrossRef]
93. Pan, P.; Wood, S.A. Solubility of Pt and Pd sulphides and Au metal in aqueous bisulphide solutions. II. Results at 200° to 350 °C and saturated vapour pressure. *Miner. Deposita* **1994**, *29*, 373–390. [CrossRef]



© 2018 by the authors. Licensee MDPI, Basel, Switzerland. This article is an open access article distributed under the terms and conditions of the Creative Commons Attribution (CC BY) license (http://creativecommons.org/licenses/by/4.0/).